RESEARCH ARTICLE

Influence of Darcy-Forchheimer Effects on 3D MHD Rotating Flow of Casson Hybrid Nanofluid with Velocity Slip and Convective Boundary Conditions

Waqas Ahmad[1,*]

[1] Department of Physical and Numerical Sciences, Qurtuba University of Science and Information Technology, Peshawar 25100, Pakistan

Abstract

In order to improve heat transfer efficiency, it is essential to examine that MHD hybrid nanofluid flows behave under convective and slip boundary conditions. Researchers have looked at a variety of factors when adding hybrid nanofluids to these flows, including Forchheimer number, radiation, magnetic fields, Biot number, and the Joule heating. The novelty of the current study lies in investigating the consequences of Casson fluid in the Darcy Forchheimer flow of a three-dimensional rotating hybrid nanofluid, which have not been thoroughly covered in the literature. This includes combinations of heat sources/sinks, magnetic parameters, and radiation absorption as well as convective conditions, slip boundary conditions, and Joule heating. By shedding light on these specific components, this endeavor seeks to bridge this knowledge gap. Hybrid nanofluids disperse two distinct nanoparticles in a fluid to increase heat conductivity for industrial purposes. The bvp5c approach is used to solve the resulting system after converting non-linear PDEs into non-linear ODEs with similarity variables. The velocity pattern falls with increasing magnetic, suction, and slip parameters, however the sheet temperature profile rises with increasing Eckert and radiative values. The research discovered that a stretched sheet's temperature increases with a larger magnetic field, whereas a shrinking sheet has the reverse effect. Detailed explanations of the numerical data accompanying the skin friction coefficient and local Nusselt number graphs for various parameter values are provided. This work uses a new non-Newtonian three-dimensional model that offers more authentic and precise visualizations of heat transport and fluid movement than traditional two-dimensional simulations. This study, in contrast to other studies, considers the dispersion of Hybrid nanofluid, three-dimensional flow, and water as the regular fluid.

Keywords: hybrid nanofluids, casson fluid, MHD, velocity slip, Joule heating, darcy-forchheimer.

Submitted: 13 September 2025
Revised: 22 November 2025
Accepted: 25 November 2025
Published: 17 January 2026

Vol. 2, **No.** 1, 2026.
10.62762/JAM.2025.945696

***Corresponding author:**
✉ Waqas Ahmad
waqas64065@gmail.com

Citation
Ahmad, W. (2026). Influence of Darcy-Forchheimer Effects on 3D MHD Rotating Flow of Casson Hybrid Nanofluid with Velocity Slip and Convective Boundary Conditions. *ICCK Journal of Applied Mathematics*, 2(1), 44–63.

© 2026 by the Author. Published by Institute of Central Computation and Knowledge. This is an open access article under the CC BY license (https://creativecommons.org/licenses/by/4.0/).

Nomenclature

C_p	Specific heat $(J \cdot Kg^{-1} \cdot K^{-1})$
Bi	Biot number
β_0	Casson parameter
Ec	Eckert number
β	Slip parameter
Fr	Darcy–Forchheimer number
K	Porous medium
S	Suction parameter
M	Magnetic parameter
Nu_x	Nusselt number
Pr	Prandtl number
q_r	Thermal radiation heat flux $(W \cdot m^{-2})$
λ	Stretching Shrinking parameter
γ	Ratio parameter
R_d	Thermal radiation parameter
ω	Rotation Parameter
Re	Reynolds number
Q	Heat source/sink parameter
Re_x	Local Reynolds number
C_f	Skin friction coefficient
T_w	Temperature of surface (K)
T	Temperature of fluid (K)
T_∞	Temperature at free-stream (K)
u, v, w	Fluid velocity components (m/s)
x, y, z	Cartesian coordinates

Greek letters

ϕ	Nanoparticle's volume fraction
η	Similarity variable
k_f	Thermal conductivity
U_f	Kinematic Viscosity
μ_f	Viscosity
ρ_f	Density of fluid
$(\rho C_p)_f$	Heat Capacitance
$\theta(\eta)$	Dimensionless temperature

Subscripts

f	Base fluid
hnf	Hybrid Nanofluid
o	Reference condition
∞	Condition at infinity in the y-axis
w	wall

Abbreviations

ODEs	Ordinary differential equations
PDEs	Partial differential equations
BCs	Boundary conditions
BL	Boundary layer
BLT	Boundary layer theory
CBLT	Convective Boundary layer theory
BVPs	Boundary value problems
MHD	Magnetohydrodynamics
HNF	Hybrid nanofluid
NF	Nanofluid
HAM	Homotopy Analysis Method

1 Introduction

Nanofluid, which has superior conduction to the base fluid, is produced when water (low thermal conductivity) and nanoparticles (less than 100 nm , high thermal conductivity) are combined. Primary fluids like ethylene glycol, water, or oil, as well as nanoparticles (oxides, metals, carbon nanotubes, or carbides) are of increasing interest to researchers for thermal applications like microelectronics. They are used in devices including fuel cells, engines, and freezers, as well as in industries like electrical, chemical, pharmaceutical, and oil cooling. Dey et al. [1] use nanoparticles to enhance heat transfer from heated areas. Makinde and Aziz [2] investigated the boundary layer flow of a nanofluid past a stretching sheet with a convective boundary condition, analyzing heat transfer characteristics under various thermal scenarios. Malvandi et al. [3] analyzed thermophoresis and Brownian motion effects on heat transfer enhancement during film boiling of nanofluids over a vertical cylinder. In a revolving permeable tube, viscoelastic dusty nanofluids containing small diamonds were examined by Ullah et al. [4]. The non-dimensional PDEs are then solved using a particular process called the Poincare Light-Hill technique. It demonstrated whenever the magnetic field and suction parameter rise, the nanofluid's velocity decreases. Ishak et al. [5] examined how radiation impacted the passage of HNFs towards both stationary and movable wedges in an inclined magnetohydrodynamics mixed convection boundary layer. Waqas et al. [6] studied the Darcy–Forchheimer relation in SWCNT–MWCNT and H_2O nanofluids, examining the influence of carbon nanotubes on thermal and flow characteristics, with skin friction and Nusselt number evaluated under various conditions. Mahian et al. [7] discussed how nanofluids may

be used in a number of fields, including energy conservation, and how they might reduce the ecological impact of energy supplies. Daniel et al. [8] investigated how the flow of MHD NF's through a porous nonlinear stretching/shrinking platform is affected by slip and convective circumstances. He studied that impact of mass, heat with convection BCs, stretching/shrinking parameters, surface slip, thermal radiation, viscosity and Joule heating, electric and magnetic fields, and more. Nandy and Mahapatra [9] analyzed that the MHD stagnation flow of a nanofluid on a stretching/shrinking medium under convective BCs is affected by sliding, heat generation, and absorption factors. The results demonstrate that velocity for the stretched sheet falls when magnetic (M) and slip (δ) parameters increase, even while temperature and nanoparticle concentration increase. Higher fluid temperatures are also a result of larger heat source characteristics.

In order to generate hybrid nanofluids, this new generation of nanofluids mixes two types of scattered nanoparticles in fundamental fluids. This novel concept offers unique properties for heat transfer applications in fields such as microelectronics, energy systems, hybrid engines, pharmacy, engine cooling, automobile heating, home refrigeration, chillers, nuclear reactor cooling, heat exchangers, machining, and space technology [10]. Aly and Pop [11] investigated a 2-D MHD HNF across a stretched and thinned plate using suction and BCs. By increasing the percentage of Cu nanoparticles, suction, and magnetic parameters for an expanding/contracting sheet, the results demonstrated that the addition of Cu nanoparticles to Al_2O_3/water assisted in cooling the hybrid nanofluid.

Waini et al. [12] Studied the energy movement in a 2-D steady HNFs with a layer that expands and contracts exponentially. The results demonstrated, when radiation impacts were amplified, the temperature rose in both solutions. The temperature, however, climbed as the magnetic parameter value grew in the second solution while falling in the first. Waini et al. [13] investigated the stretching and contracting properties of a sheet-induced HNF, which was produced by combining copper nanoparticles with an Al_2O_3/water nanofluid. In unsteady MHD flow on a stretched surface, heat and mass transport were examined in connection with suction, chemical reactions, slip conditions, and thermal radiation. Ishak et al. [15] investigated that impacts of suction/injection through a vertical wall with heat flow on the viscous MCBL. Findings indicated that the movement of the field and heat exchange frequency across the plate are significantly altered by fluid injection or suction through the boundary surface. The ratios of heat transmission and skin friction are sometimes increased by suction.

Magnetohydrodynamics (MHD), the study of electrically charged fluids, including seawater, liquid metals, plasmas, and electrolytes is necessary to manage fluid flow. Magnetic fields are used in many technological processes and geophysical research initiatives. Furthermore, MHD is used in magnetic drug targeting for cancer therapy. Anuar et al. [14] investigated the MHD stagnation point flow of Cu–Al_2O_3/water hybrid nanofluid past a stretching/shrinking sheet in the presence of homogeneous-heterogeneous reactions and convective boundary conditions. The effects of heat and mass transfer on fluid flow have received a lot of attention lately. Examples of processes that include simultaneous heat and mass transmission include drying, evaporation from water surfaces, flow in desert coolers, and energy transfer in cooling towers. Abdollahi et al. [16] numerically investigated heat transfer and fluid flow between parallel surfaces under hybrid nanofluid suction and injection conditions. Heat generation is necessary for the cooling of nuclear fuel debris, the disposal of radioactive waste underground, fluid disassociation in packed-bed reactors, and food storage. In their research, Alreshidi et al. [17] examined the MHD three-dimensional nanofluid flow over a porous rotating disk with velocity slip conditions and Joule dissipation, investigating the effects of Brownian motion and thermophoresis on heat and mass transfer characteristics. Kataria and Mittal [18] investigated how a nanofluid's convective flow via a porous media across an oscillating vertical surface was impacted by an electromagnetic field. Shah et al. [19] A uniform internal heat source and Darcy's equation for momentum transmission in the porous medium are both included in the mathematical model. Waini et al. [20] investigated the flow and heat transfer of a hybrid nanofluid past a permeable moving surface, demonstrating that the magnetic parameter and radiation significantly influence the thermal boundary layer thickness and heat transfer rate. Manjunatha et al. [21] The influence of radiation on unsteady, free-convective nanofluid flow in a rotating system with a heat source and magnetic field are investigated in this work. The perturbation method is used to

solve the governing equations analytically. Krishna and Reddy [22] examined the impact of unsteady magnetohydrodynamics free convective boundary layer flow through a porous material past a moving vertical plate with a heat source and chemical reaction. A simple technique was used to solve these equations, and a number of parameters were explained and shown. Temperature, velocity, concentration, and skin friction profiles were displayed graphically and supported by tables. Slip motion significantly affects surfaces such as lobbing, especially primary slip in fluids in granular phases such as water-and-oil mixtures, emulsions, and egg yolks. Artificial heat tubes and internal cavity cleaning are two examples of how this phenomena is used in engineering and technology.

The extensive use of non-Newtonian liquids in engineering and production accounts for their significance in fluid mechanics. Sauce, molten polymers, paints, ketchup, honey, blood, shampoos, and polymeric fluids are examples of substances that behave in a non-Newtonian manner. Among these fluids are Casson fluid, power-law fluid, and pair stress fluid. Ali et al. [23] examined the effects of wall temperature and convective conditions on the heat transfer evaluation of an unstable MHD slip flow of ternary hybrid Casson fluid across a dynamic stretching disk encased in a porous material. Following the application of the proper transformations, the governing PDEs changed into ODEs and evaluated using the Keller-box technique. Variations in radiation do not directly affect fluid velocity in forced convection. However, fluid velocity decreases in opposing flow when the radiation parameter rises, but the converse happens in helpful flow. Additionally, it was demonstrated that fluid concentration and velocity increase with positive chemical reactions and decrease with destructive chemical reactions. The significance of slip and convective circumstances for non-Newtonian HNF movement across a bi-directional stretching surface were studied by Hussain et al. [24]. The HAM approach was applied to simplify the leading nonlinear PDEs after they had been transformed into ODEs using similarity technique. The results demonstrate that the Casson component has less of an effect on the velocity pattern along the x and y - axes. The non-Newtonian fluid flow with Soret Dufour effect and activation energy is examined. Ahmad et al. [25] examined how non-Newtonian fluid movement towards a radiative moving sheet is affected by temperature and velocity slip circumstances, mixed convection, accelerated transport processes, and chemical reactions. By increasing the free convection parameters Gr , and Gc the study shows that the velocity profile improves. Nevertheless, it is decreased by the mass suction parameter, velocity slip, magnetic field, and Casson parameter. Furthermore, a higher temperature profile is produced by raising the Gc, Nb, Nt, Rd , Gc, Nb, Nt, Rd , and θ_w parameters, whereas the converse is true for the β, Gr, S , and ϵ factors. Ibrahim and Anbessa [26] studied ion and Hall slip phenomena in 3-D MHD Casson mixed convection nanofluid flow. Similarity transformations converted the governing PDEs into a system of linked nonlinear ODEs, which were then numerically solved using the spectrum relaxation technique (SRM). The results show that increasing the magnetic field and Casson fluid factors causes velocity distribution to decrease in both the x & y - directions, but increasing the ion, Hall slip, and mixed convection variables has the opposite effect. Furthermore, the temperature profile is improved by improvements in the heat source and radiation characteristics.

Many researchers are now interested in hybridized fluid motion across permeable porous surfaces because of its wide variety of possible uses. There may be uses for flow over these surfaces in solar energy, nuclear engineering, environmental science, and materials research. It is common practice to apply Darcy's law to comprehend this kind of movement, by Alnahdi and Gul [27] despite the fact that it is not always correct, it is nonetheless extensively used. Forchheimer improved the permeability estimation by creating a second-order polynomial to be utilized in the momentum equation to adjust for the influence of inertia. Zainal et al. [28] effects of slip near the stagnation point migration of hybrid nanofluids via unstable mixed convection. Asghar et al. [29] examined how an HNF with magnetized mixed convection is impacted by variables like velocity slip & heat generation/absorption.

Usman et al. [30] investigated how a magnetohydrodynamics HNF moves across a surface that is becoming more and more expandable in relation to the impacts of slip conditions and Darcy-Forchheimer theory. The semi-analytical HAM was used to the system of dimensionless ODEs in order to obtain the result. The relationship between Nusselt number, skin friction, and a variety of hybridization fluid characteristics was demonstrated using bar charts. It was discovered that the Darcy-Forchheimer medium,

suction parameter, and no-slip condition improved the hybridized fluid's temperature profile. Haider et al. [31] examined that a HNF moved through a porous material with different Darcy-Forchheimer properties. In regards to local heat transmission amount, it was shown that the Ti_3O_2 nanofluid behaved better than the hybrid nanofluid. Furthermore, the findings demonstrate that when the thermal radiation variable rises, so does the local Nusselt number. Abu Bakar et al. [32] examined how an HNF moved with second-order velocity slip in a DF porous material over a permeability contracting surface. A visual representation of skin friction coefficient, velocity, temperature, and Nusselt numbers profiles in relation to physical parameters including Darcy-Forchheimer number, suction, radiation, permeability of porous media, shrinkage, and nanoparticle quantity fraction was created using MATLAB's bvp4c solver. The study found that the HNF performed better with regard to transfer of mass and heat ratios than the conventional mono-nanofluid.

Ali et al. [33] examined the influence of a DF porous medium with radiative flow of a cross-ternary HNF (Ag/CMC-water, TiO_2 , and MoS_2) over a stretched cylinder utilizing entropy-minimization. The impacts of several variables on concentration, and temperature distributions, flow velocity, Bejan number, and entropy production were thoroughly investigated in this work. It was shown that as the Weissenberg number & porosity variables rise, the $f'(\eta)$ figure decreases. Ganesh et al. [34] studied that a shrinking-stretching porous surface was affected by slip circumstances and the thermal stratification of nanofluid. Seddeek [35] examined the mixed convective laminar dissipation is affected by Darcy-Forchheimer flow. Saeed et al. [36] Analyzing heat transfer and DF magnetohydrodynamics HNF flow over a porous stretched cylinder were the main objectives of this effort. Alzahrani et al. [37] investigated that a HNF traveling across a flat layer was affected by solar radiation using a DF permeable material. Alrabaiah et al. [38] explored, using computational simulations, the Darcy-Forchheimer infrared HNF flow across a curved, slippery materials. A computational calculation of the associated coupled of nonlinear equations was performed using the parametric continuation method (PCM). Dissipation's impact on the velocity and heat transmission behavior of MHD flow when heat generation or absorption over a convective surface fluctuates has not, as far as we know, been investigated. The BVP5C-based shooting approach was used to overcome the issue. The incorporation components as a function of temperature and velocity are represented graphically by the slip, Casson, and Grashof parameters, as well as by the radiative, magnetic, Biot, Prandtl, and Eckert numbers, and changeable heat production or utilization quantities. A table was created by analyzing the numerical values of the identical parameters on the skin friction factor and Nusselt number.

2 Problem statement

When creating a mathematical model, take into consideration the following assumptions:

1. A three-dimensional flow field is assumed by the incompressible flow across a continuous stretching/shrinking sheet.

2. The HNF (copper and alumina) are considered with base fluid (water).

3. Provide the velocities at the wall along the $x\&y$ -axes with the following assumptions: $u_w(x) = ax$, and $v_w(x) = ax$, accordingly, assuming a is a positive constant.

4. The novelty of this work is non-Newtonian fluid (Casson), Rotating, and Darcy-Forchheimer flow is taken into account.

5. The xy -planes show stretching or contracting surfaces under Joule heating, thermal radiation, & slip boundary conditions whereas the flow field domain is located in the area $z \geq 0$.

6. Heat transfer coefficients h_f are produced by the application of a convective condition at the bottom of the sheet, which is caused by the constant temperature T_f.

7. However, the effects of nanoparticle aggregation brought on by hybridization are ignored.

8. Furthermore, perpendicular to the plane, a high magnetic flux density B_0 homogeneous magnetic field is supplied.

As described by Devi and Devi [39], Khashi'ie et al. [40], Kumar et al. [41], and Ahmed et al. [42]. The following are the non-linear PDEs that control the conservation of mass, momentum, and energy:

$$\frac{\partial u}{\partial x} + \frac{\partial \nu}{\partial y} + \frac{\partial w}{\partial z} = 0 \tag{1}$$

Table 1. Wahid & Aldhafeeri et al. [44, 45] mathematical calculations for the thermophysical properties of HNFs.

Density	$\rho_{hnf} = \rho_{s1}\phi_1 + \rho_{s2}\phi_2 + \rho_f(1-\phi_{hnf}) \quad \text{where} \quad \phi_{hnf} = \phi_1 + \phi_2$
Thermal Conductivity	$\frac{k_{hnf}}{k_f} = \frac{\frac{\phi_{s1}k_{s1}+\phi_{s2}k_{s2}}{\phi_{hnf}} + 2k_f + 2(\phi_{s1}k_{s1}+\phi_{s2}k_{s2}) - 2k_f\phi_{hnf}}{\frac{\phi_{s1}k_{s1}+\phi_{s2}k_{s2}}{\phi_{hnf}} + 2k_f + (\phi_{s1}k_{s1}+\phi_{s2}k_{s2}) - k_f\phi_{hnf}}$
Dynamic Viscosity	$\frac{\mu_{hnf}}{\mu_f} = \frac{1}{(1-\phi_{hnf})^{2.5}}$
Heat capacity	$(\rho C_p)_{hnf} = (1-\phi_{hnf})(\rho C_p)_f + \phi_{s1}(\rho C_p)_{s1} + \phi_{s2}(\rho C_p)_{s2}$
Electrical Conductivity	$\frac{\sigma_{hnf}}{\sigma_f} = \frac{\frac{\phi_{s1}\sigma_{s1}+\phi_{s2}\sigma_{s2}}{\phi_{hnf}} + 2\sigma_f + 2(\phi_{s1}\sigma_{s1}+\phi_{s2}\sigma_{s2}) - 2\sigma_f\phi_{hnf}}{\frac{\phi_{s1}\sigma_{s1}+\phi_{s2}\sigma_{s2}}{\phi_{hnf}} + 2\sigma_f + (\phi_{s1}\sigma_{s1}+\phi_{s2}\sigma_{s2}) - \sigma_f\phi_{hnf}}$

$$u\frac{\partial u}{\partial x} + \nu\frac{\partial u}{\partial y} + w\frac{\partial u}{\partial z} - 2\Omega\nu = \frac{\mu_{hnf}}{\rho_{hnf}}\left(1+\frac{1}{\beta}\right)\frac{\partial^2 u}{\partial y^2} - \frac{\sigma_{hnf}}{\rho_{hnf}}\mathrm{B}_0^2 u - \frac{\mu_{hnf}}{\rho_{hnf}k}u - \frac{C_b}{x\sqrt{K}}u^2 \tag{2}$$

$$u\frac{\partial \nu}{\partial x} + \nu\frac{\partial \nu}{\partial y} + w\frac{\partial \nu}{\partial z} + 2\Omega u = \frac{\mu_{hnf}}{\rho_{hnf}}\left(1+\frac{1}{\beta}\right)\frac{\partial^2 \nu}{\partial z^2} - \frac{\sigma_{hnf}}{\rho_{hnf}}\mathrm{B}_0^2 \nu - \frac{\mu_{hnf}}{\rho_{hnf}k}\nu - \frac{C_b}{x\sqrt{K}}\nu^2 \tag{3}$$

$$(\rho C_p)_{hnf}\left(u\frac{\partial T}{\partial x} + \nu\frac{\partial T}{\partial y} + w\frac{\partial T}{\partial z}\right) = \left(k_{hnf} + \frac{16\sigma T_\infty^3}{3k}\right)\frac{\partial^2 T}{\partial z^2} + \sigma_{hnf}B_0^2\left(u^2+\nu^2\right) + Q_0(T-T_\infty) \tag{4}$$

along with BCs [40]:

$$\begin{aligned} &u = u_w\lambda + \beta_0\frac{\partial u}{\partial z}, \\ &\nu = \nu_w(y)\lambda + \beta_0\frac{\partial \nu}{\partial z}, -k_{hnf}\frac{\partial T}{\partial z} = h_f\left(T_f - T\right), \\ &w = w_0 \quad at \quad y = 0 \\ &u \to 0, \nu = 0, T \to T_\infty, \quad as \quad y \to \infty. \end{aligned} \tag{5}$$

With these arrangements, the schematic representation of the problem is illustrated in Figure 1, which shows the flow configuration and boundary conditions.

Here, K shows porous medium, B_0^2 shows Magnetic field, $\lambda > 0$ for stretching sheet, $\lambda = 0$ for static sheet, $\lambda < 0$ for shrinking sheet, T represents fluid temperature, β_0 represent slip parameter, $u\&v$ represents velocity components in x & y - directions, T_w , & T_∞ represents at wall & far temperature, q_r shows Radiation, Q shows Heat source/sink, h_f for heat transfer coefficient, T_f for constant temperature. $w_0 = -\sqrt{av_f}S$, while $w_0 > 0$ shows injection case, $w_0 < 0$ represent suction.

Therefore, the mathematical connection for k_{hnf} , σ_{hnf} , ρ_{hnf} , μ_{hnf} , and $(\rho C_p)_{\mathrm{hnf}}$ observable in the accompanying Table 1, and the thermophysical properties of the base fluid (water) and nanoparticles (Al_2O_3 and Cu) are provided in Table 2.

Table 2. Thermophysical properties of base fluid and nanoparticles adopted from [46].

Property	Al_2O_3	Cu	H_2O
k (W/mK)	40	400	0.613
ρ (Kg/m^3)	3970	8933	997.1
σ (S/m	35×10^6	59.6×10^6	5.5×10^{-6}
C_p (J/kgK)	765	385	4179
Pr	6.2	-	-

Introduce the following transformations:

$$\begin{aligned} &\eta = z\sqrt{\frac{a}{\nu_f}}, \theta(\eta) = \frac{T-T_\infty}{T-T_\infty}, \nu = ayg'(\eta), \\ &w = -\sqrt{a\nu_f}[f+g], u = axf'(\eta). \end{aligned} \tag{6}$$

Inserting Eq. (5) towards Eq. (2)-(4), the following result is obtained.

After modification, Eqs. (2), and (3) may take the following form:

$$\left(1+\frac{1}{\beta}\right)f''' - \frac{\rho_{hnf}/\rho_f}{\mu_{hnf}/\mu_f}\left((1+Fr)f'^2 - (f+g)f'' + 2\gamma\omega g'\right) - \left(\frac{\sigma_{hnf}/\sigma_f}{\mu_{hnf}/\mu_f}M + K\right)f' = 0 \tag{7}$$

$$\left(1+\frac{1}{\beta}\right)g''' - \frac{\rho_{hnf}/\rho_f}{\mu_{hnf}/\mu_f}\left((1+\gamma Fr)g'^2 - (f+g)g'' + \frac{2\omega}{\gamma}f'\right) - \left(\frac{\sigma_{hnf}/\sigma_f}{\mu_{hnf}/\mu_f}M + K\right)g' = 0 \tag{8}$$

$$\frac{K_{hnf}}{K_f}\theta'' + \frac{4R_d}{3}\theta'' + \mathrm{Pr}\frac{(\rho c_p)_{hnf}}{(\rho c_p)_f}\left(f\theta' + g\theta'\right) + \frac{\sigma_{hnf}}{\sigma_f}\mathrm{Pr}\,M\left(Ec_x f'^2 + Ec_y g'^2\right) + \mathrm{Pr}\,Q\theta = 0 \tag{9}$$

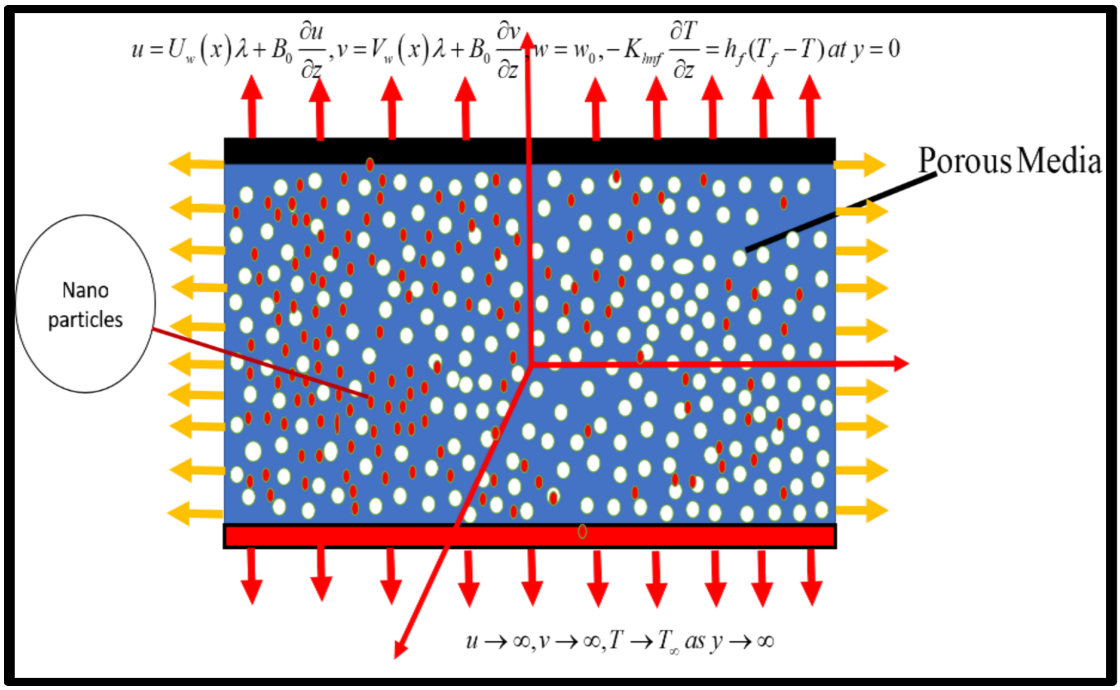


Figure 1. Flow configuration [43].

Table 3. Non-dimensional variable are discussed as:

S. No.	Name of the parameter	Expression	Range
1	Porosity parameter	$K = v_f/ka$	0.5
2	Darcy-Forechheimer	$Fr = C_b/\sqrt{k}$	2
3	Rotation Parameter	$\omega = \Omega/a$	0.5
4	Ratio Parameter	$\gamma = y/x$	0.5
5	Magnetic Parameter	$M = \sigma_f B_0^2/\rho_f a$	1
6	Radiation Parameter	$Rd = 4\sigma^* T_\infty^2/k^* k_f$	0.5
7	Prandtl number	$\Pr = (\mu c_p)_f/k_f$	6.2 [42]
8	Heat source/sink parameter	$Q = Q_0/(\rho c_p)_f$	1
9	Eckert number	$Ec = u_w^2/(c_p)_f(T_w - T_\infty)$	0.1
10	Slip Parameter	$\beta = \sqrt{a/v_f}\beta_0$	0.5
11	Biot number	$Bi = h_f/k_f\sqrt{v_f/a}$	0.1
12	Suction Parameter	S	2
13	Stretching/Shrinking Parameter	λ	$-1 \le \lambda \le 1$
14	Casson Parameter	β_0	0.2
15	Density, Thermal Conductivity, Viscosity, Heat capacity, Electrical conductivity	$w_1 = \frac{\mu_{hnf}}{\mu_f}, w_2 = \frac{\rho_{hnf}}{\rho_f}, w_3 = \frac{(\rho C_p)_{hnf}}{(\rho C_p)_f}, w_4 = \frac{\sigma_{hnf}}{\sigma_f}, w_5 = \frac{k_{hnf}}{k_f}.$	

together with the BC's

$$\begin{aligned} &f'(0) = \lambda + \beta f''(0), g'(0) = \lambda + \beta g''(0), \\ &f(0) + g(0) = S, -\frac{K_{hnf}}{K}\theta'(0) = Bi\,(1 - \theta(0)), \\ &f'(\infty) \to 0, g'(\infty) \to 0, \theta(\infty) \to 0. \end{aligned} \quad (10)$$

where λ is the stretching/shrinking parameters, M represent magnetic field, K represent porous medium, Rd represents radiation, β is the velocity slip parameter, Bi shows the Biot number, Q is the heat source/sink, $\Pr$ represents Prandtl number, and Ec_x and Ec_y is the Eckert number along x and y direction, that are understood as in Table 3.

3 Engineering quantities

$$\begin{aligned} &C_{f_x} = \frac{T_w}{\rho_f u_w^2}, C_{f_y} = \frac{T_w}{\rho_f u_w^2}, \quad \text{where} \quad T_w = \mu\left(\frac{\partial u}{\partial y}\right)_{y=0} \\ &Nu_x = \frac{x q_w}{k_f\,(T_w - T_\infty)} + (q_r)_{y=0} \quad \text{where} \quad q_w = -k\left(\frac{\partial T}{\partial y}\right)_{y=0} \end{aligned} \quad (11)$$

The non-dimensionalized expression for C_{f_x} , C_{f_y} & Nu_x takes the following form:

$$
\begin{aligned}
&C_{f_x} R_{e_x}^{1/2} = \frac{\mu_{hnf}}{\mu_f}\left(1+\frac{1}{\beta}\right) f''(0),\\
&C_{f_y} R_{e_x}^{1/2} = \frac{\mu_{hnf}}{\mu_f}\left(1+\frac{1}{\beta}\right) g''(0),\\
&Nu_x R_{e_x}^{-\frac{1}{2}} = -\frac{K_{hnf}}{K_f}\left(1+\frac{4}{3}Rd\right)\theta'(0),\\
&where \quad R_{e_x}^{\frac{1}{2}} = x\left(\frac{a}{\nu}\right)^{\frac{1}{2}}.
\end{aligned} \tag{12}
$$

4 Numerical Methodology

In this study, the nonlinear ODEs (7), (8), and (9) are modeled with BCs (10), using the BVP5C computational solver in MATLAB. These three nonlinear ordinary differential equations have temperature and velocity figures of order two and three, respectively.

$$
\begin{aligned}
f''' = \frac{\beta w_2}{w_1}\Big((1+Fr)\,f'^2 + 2\gamma\omega g' - (f+g)\,f''\\
+\left(\frac{w_4}{w_1}M + K\right) f'\Big)
\end{aligned} \tag{13}
$$

$$
\begin{aligned}
g''' = \frac{\beta w_2}{w_1}\left((1+Fr)\,g'^2 + \frac{2\gamma}{\omega}f' - (f+g)g''\right.\\
\left.+\left(\frac{w_4}{w_1}M + K\right) g'\right)
\end{aligned} \tag{14}
$$

$$
\begin{aligned}
\theta'' = \frac{1}{\left(w_5 + \frac{4Rd}{3}\right)}\left(-\Pr w_3(f\theta' + g\theta')\right.\\
\left.-w_4 \Pr M(Ecf'^2 + Ecg'^2) - \Pr Q\theta\right)
\end{aligned} \tag{15}
$$

To solve this set of nonlinear differential equations (13), (14), and (15) using the BVP-5C approach, we first convert them to the coupled of 1^{st} order ODEs.

Hence, one may assume that

$$
\begin{aligned}
f = S(1), f' = S(2), f'' = S(3), g = S(4),\\
g' = S(5), g'' = S(6), \theta = S(7), \theta' = S(8).
\end{aligned} \tag{16}
$$

Following that, the five first-order differential equations that were transformed are

$$
\begin{pmatrix}
f' = S(2),\\
f'' = S(3),\\
f''' = \frac{\beta_0 w_2}{w_1}\left((1+Fr)\,S^2(2) - (S(1)+S(4))\,S(3)\right.\\
\quad \left.+2\gamma\omega S(5) + \left(\frac{w_4}{w_1}M + K\right) S(2)\right)\\
g' = S(5),\\
g'' = S(6),\\
g''' = \frac{\beta_0 w_2}{w_1}\left((1+Fr)\,S^2(5) - (S(1)+S(4))\,S(6)\right.\\
\quad \left.+2\frac{2\gamma}{\omega}S(2) + \left(\frac{w_4}{w_1}M + K\right) S(5)\right)\\
\theta' = S(8),\\
\theta'' = \frac{1}{\left(w_5 + \frac{4Rd}{3}\right)}\begin{pmatrix}-\Pr w_3(S(1)S(8) + S(4)S(8))\\ -w_4 \Pr M(EcS^2(2)\\ +EcS^2(5)) - \Pr QS(7)\end{pmatrix}
\end{pmatrix}
$$

With the respective converted boundary conditions as;

$$
\begin{pmatrix}
S_a(2) - \lambda - \beta S_a(3), S_a(5) - \lambda - \beta S_a(6),\\
S_a(1) + S_a(4) - S, w_5 S_a(8) + Bi(1 - S_a(7)),\\
S_b(2), S_b(5), S_b(7)
\end{pmatrix} \tag{17}
$$

It is composed up of many differential equations that are solved simultaneously and have suitable boundary conditions. As a result, using MATLAB to enforce the BVP5C solver is now straightforward, following the residual-control-based boundary value problem framework and its higher-order extensions [47–50].

5 Results & Discussion

We have investigated numerically the 3D rotating fluid flow of an MHD Casson HNFs with radiation, magnetic field parameter, slip, Darcy–Forchheimer, and Joule heating effects. Casson parameter (β_0), heat source parameter (Q), Suction parameter (S), Biot number (Bi), porous medium (K), Darcy–Forchheimer (Fr), Eckert number (Ec), stretching/shrinking parameter (λ), slip effect (β), radiation parameter (Rd), & Prandtl number (Pr) have all been studied and their effects on the temperature and velocity distribution have been reported. Additionally, the skin friction coefficient and Nusselt number are presented to give a comprehensive understanding of the shear stress speed and heat transfer speed, respectively.

As a result, numerous industrial equipment use nanoparticles as cooling substance. In the shrinking

scenario, the temperature of the liquid particle has a bigger influence than in the stretching scenario when the fraction of hybrid nanofluid (Cu & Al_2O_3) in the basic fluid is increased. Consequently, in the stretching and shrinking cases, molecules of fluid supply more heat, correspondingly.

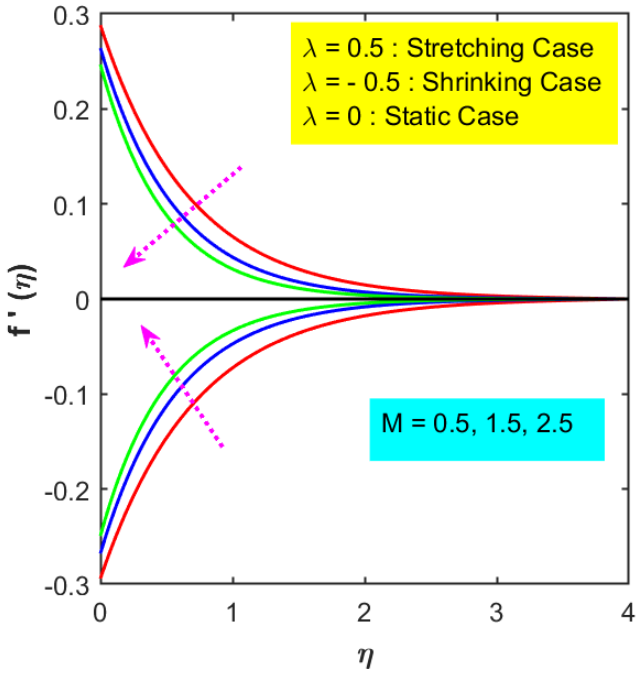


Figure 2. Variation of M on $f'(\eta)$.

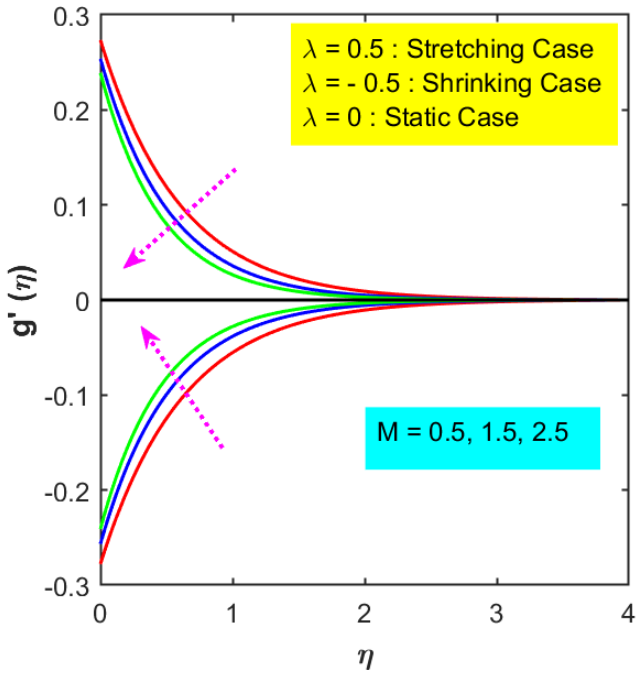


Figure 3. Variation of M on $g'(\eta)$.

For the static, stretching, and shrinking scenarios, the velocities ($f'(\eta), g'(\eta)$) profiles are influenced by the electromagnetic field variable, as shown in Figures 2 and 3. However, these velocities ($f'(\eta), g'(\eta)$) on the boundary layer appears to have the opposite impact when the magnetic field parameter is increased. It has been noted that when M increases, the fluid molecules primary velocity decreases. Lorentz's force causes the stretched sheet's resistivity to decrease with the lowest magnetic parameter value, whereas the resistivity of an electrically conducting hybrid nanofluid increases with increasing magnetic parameter values. Therefore, in the stretching ($\lambda > 0$) situation, increasing a magnetic variable results in a smaller momentum restriction layer, whereas in the shrinking ($\lambda < 0$) case, the opposite behavior is observed. A physical force that attempts to obstruct flow is the drag force, often known as Lorentz's force. Among other things, this energy is employed to regulate the flow field, which is advantageous for wires covered with electromagnetic substances and metal.

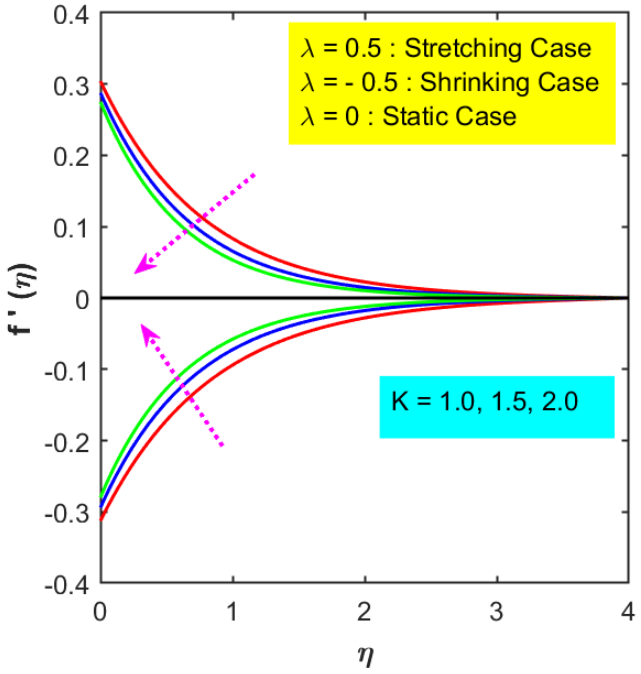


Figure 4. Variation of K on $f'(\eta)$.

Figures 4 and 5 show the both velocities profiles in relation to the porosity factor (K). A noticeable decrease in both velocities is observed as K enhanced. This trend results from normal stress increasing together with porosity, which reduces the overall depth of the boundary zone. In conclusion, the force is more efficiently transmitted to adjacent particles, accelerating them and changing the distribution of velocity [42].

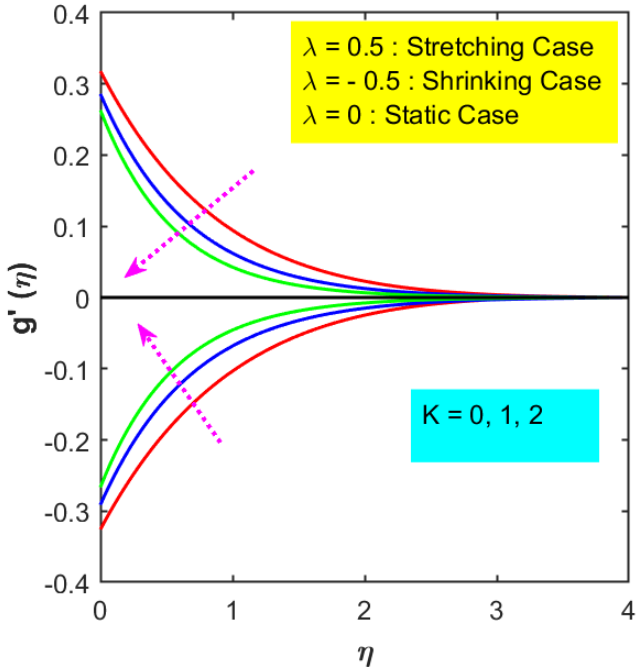


Figure 5. Variation of K on $g'(\eta)$.

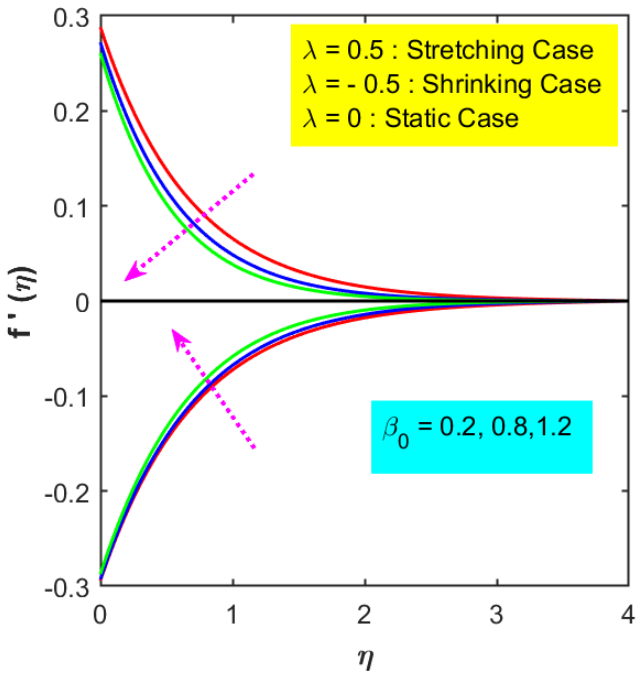


Figure 6. Variation of β_0 on $f'(\eta)$.

In both the stretching and shrinking situations, Figures 6 and 7 illustrate the effect of the Casson component (β_0) on the velocities distributions ($f'(\eta), g'(\eta)$). An increasing non-Newtonian flow impedance of the fluid is indicated by the obvious reduction in the velocity fields as the Casson variable increases. A greater Casson parameter results in a larger fluid yield stress, which makes the fluid more resistant to deformation,

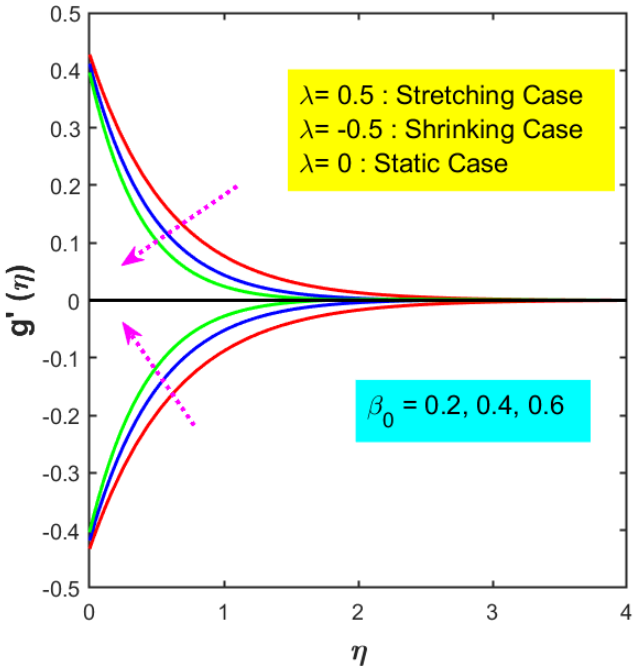


Figure 7. Variation of β_0 on $g'(\eta)$.

which causes this drop. As a result, the fluid flow slows down under stretching, decreasing the velocity profiles, while in shrinking case the opposite behavior is observed.

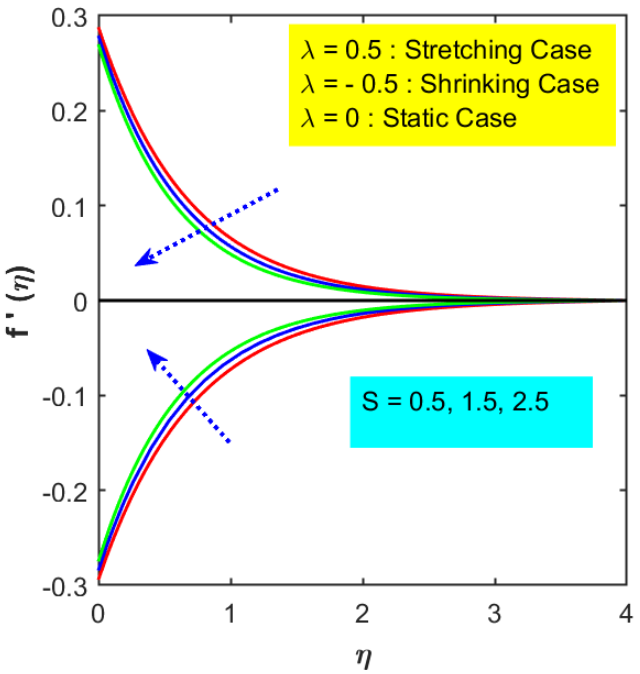


Figure 8. Variation of S on $f'(\eta)$.

Figures 8 and 9 demonstrated that the suction parameter (S) affects the patterns of velocities $(f'(\eta), g'(\eta))$ for the static, stretching, and shrinking

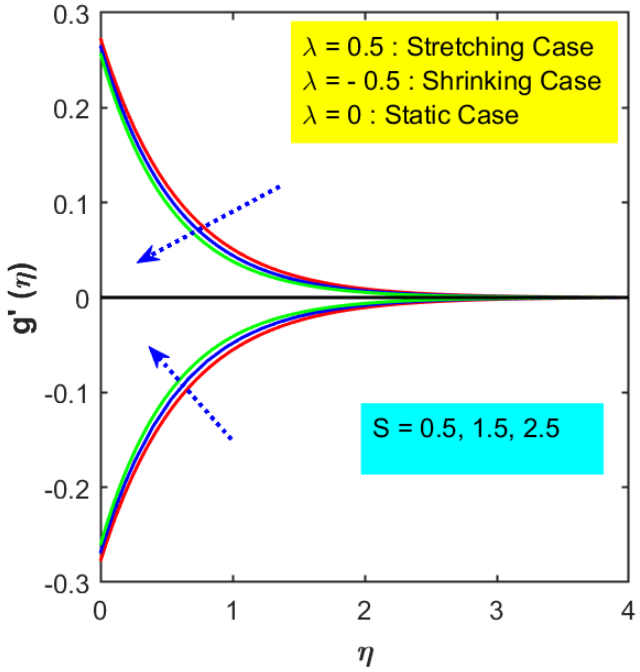


Figure 9. Variation of S on $g'(\eta)$.

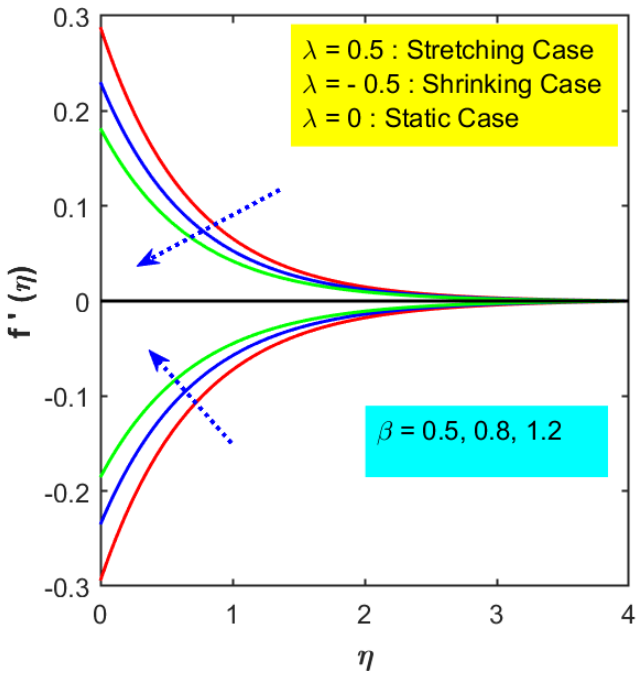


Figure 10. Variation of β on $f'(\eta)$.

scenarios. A multitude of dimensionless parameters, including the suction variable, can regulate the HNF's flow. The fluid molecules velocity is reduced in order to lessen the drag impact brought on by external flow. The major velocity profile's performance when the suction variable (S) influences the stretching or shrinking surface is seen in Figure 8. It is demonstrated that given the greatest suction over a decreasing

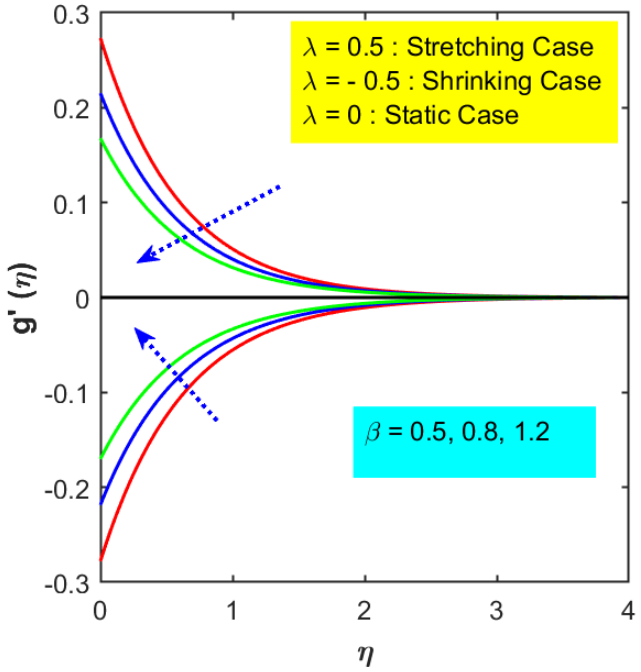


Figure 11. Variation of β on $g'(\eta)$.

surface, the primary velocity profile decreases and increases over a stretched surface. Figures 10 and 11 illustrates when the slip parameter (β) affects the distributions of velocities $(f'(\eta), g'(\eta))$ in the stretching, shrinking, and static cases. The fluid molecules experience the least amount of resistive force action at lower values of β , which subsequently causes the fluid's resistivity to steadily grow. A greater value of β causes a reduction in $f'(\eta)$ because the fluid molecules encounter resistive force from the slip component across a stretched surface. A HNFs on other hand, acts in the opposite manner over a decreasing, shrinking surface.

Figure 12 illustrates that the dimensionless temperature pattern in an HNF composed of (C_u & Al_2O_3) nanoparticles floating in water across stretching and contracting sheets is influenced by the magnetic component. The fluid molecules get more thermal energy when M has a higher influence on temperature in the decreasing instance than on the stretched surface. The depth of the thermal boundary layer increases with increasing M for the expanding sheet and decreases with increasing M for the contracting sheet. This occurs because of a drag force that is produced when the conducting fluid interacts with the nanoparticles in the magnetic field. This contact elevates the temperature figure and produces heat within the fluid. Since the NF_s temperature has a significant impact on the parameters of heat

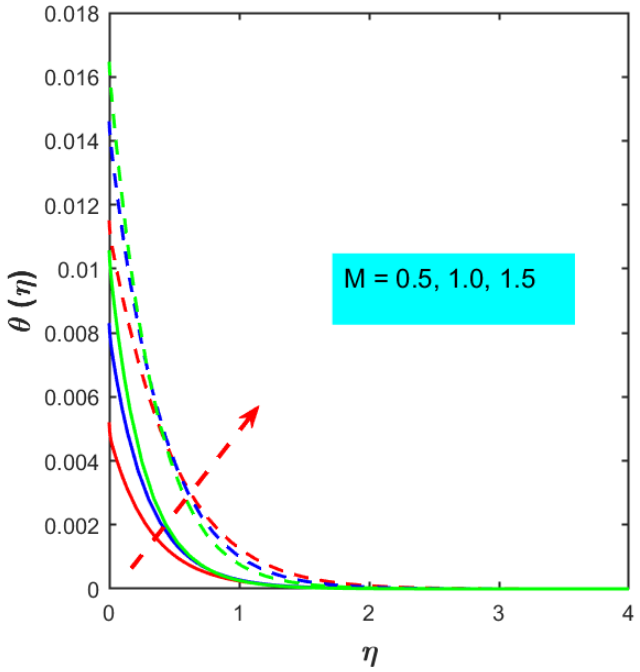


Figure 12. Variation of M on $\theta(\eta)$.

transport on the stretched sheet, regulating the fluid's temperature can improve heat transfer from the fluid's interface.

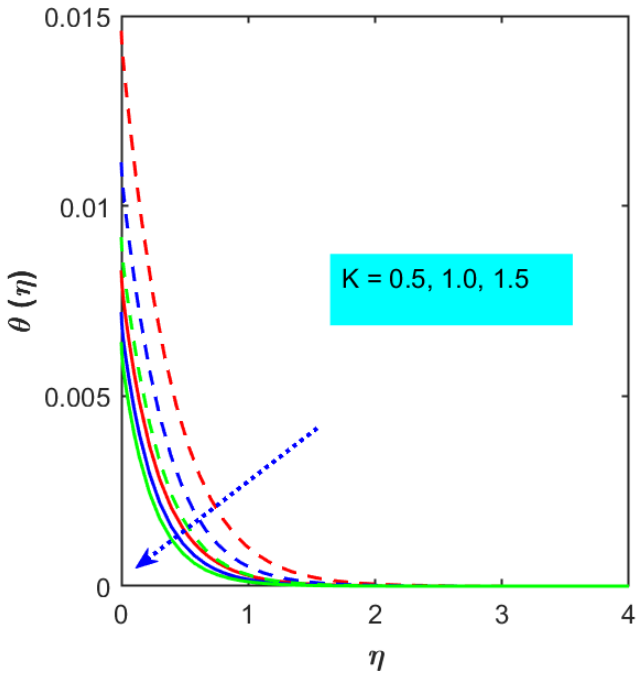


Figure 13. Variation of K on $\theta(\eta)$.

Figure 13 illustrates that temperature distributions are affected by the porosity parameter (K) in both the stretching and shrinking situations. The temperature inside the boundary layer is demonstrated to increase in the stretching scenario as the porosity parameter increases, whereas the opposite tendency is shown in the shrinking situation. This divergent behavior demonstrates the intricate relationship that exists between flow dynamics and porosity in determining heat transfer properties.

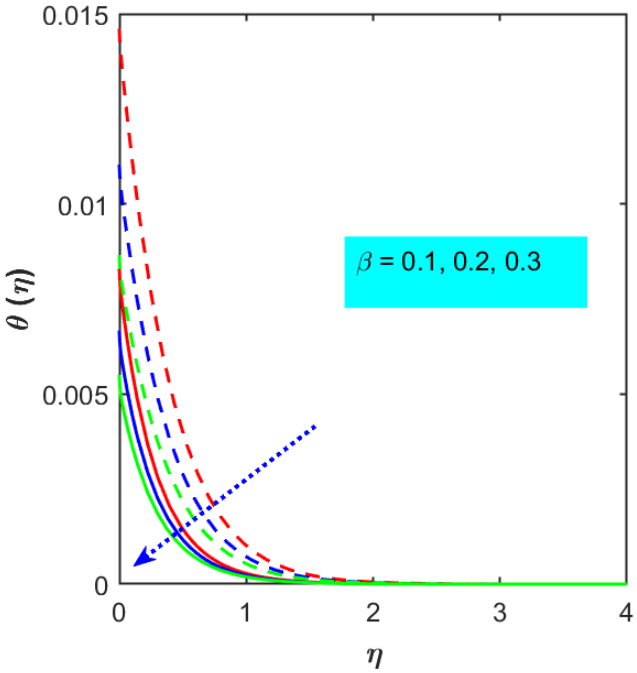


Figure 14. Variation of β on $\theta(\eta)$.

Figure 14 shows how the temperature distributions for both the stretching and shrinking illustration are affected by the slip parameter (β) . The amount of heat transfer has been shown to be impacted by reducing surface drag by raising the slip parameter. The fluid's temperature decreases because the thermal barrier surface is thinner close to the surface.

Temperature distributions for the stretching and shrinking scenarios are influenced by the suction value, as seen in Figure 15. With an increase in the suction parameter, the thermal boundary layer's thickness usually decreases. The enhanced suction action that enhances heat evacuation from the surface explains this phenomenon.

Figure 16 shows that temperature distributions for the stretching and shrinking scenario are affected by the Casson parameter (β_0) . It is demonstrated that variations in β_0 have a considerable effect on the thermal boundary layer. The temperature profile demonstrates the fluid's non-Newtonian characteristics as β_0 rises. The temperature pattern demonstrates the fluid's non-Newtonian

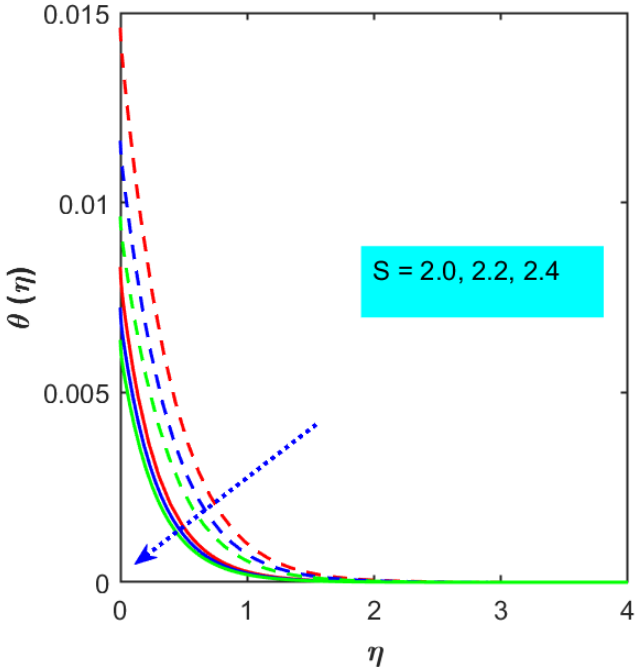


Figure 15. Variation of S on $\theta(\eta)$.

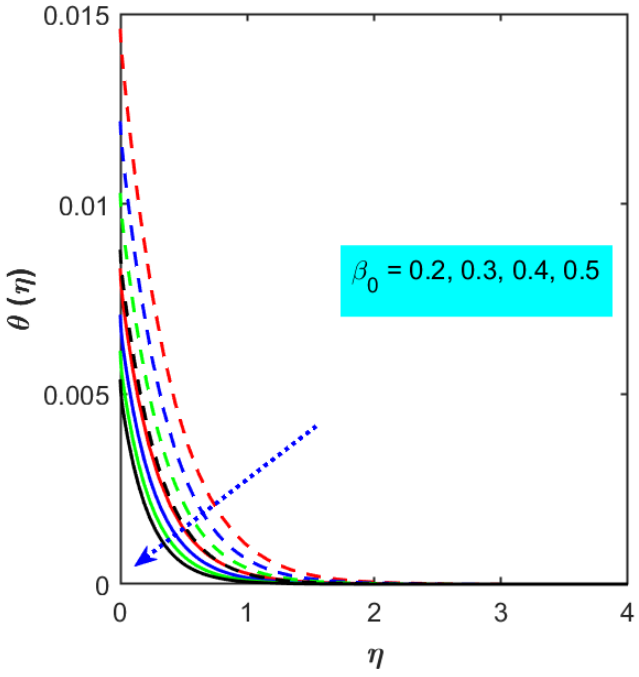


Figure 16. Variation of β_0 on $\theta(\eta)$.

characteristics as β_0 climbs.

Figure 17 illustrates that the temperature $\theta(\eta)$ for the HNFs $Al_2O_3 - Cu/H_2O$ is affected by the radiation parameter (Rd). As Rd climbs, the temperature gradually rises. This measurement shows how much thermal radiation is worth in relation to heat conduction. The primary means of heat transfer, thermal radiation, causes the environment's

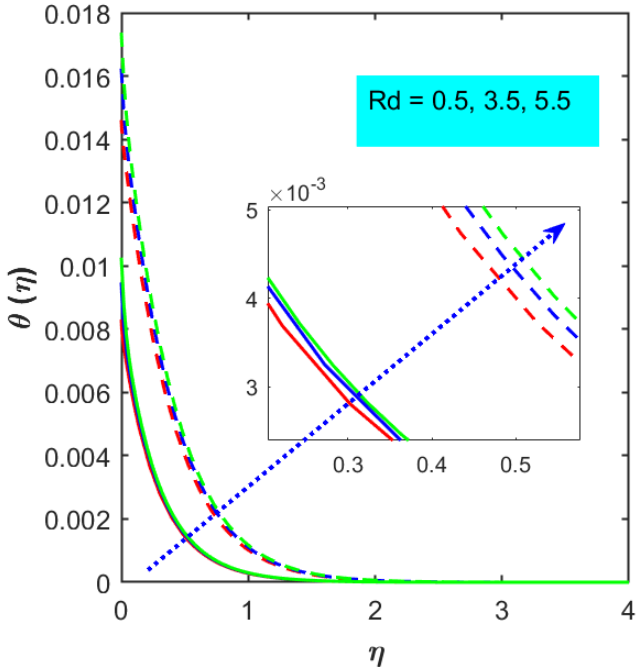


Figure 17. Variation of Rd on $\theta(\eta)$.

temperature to increase because, as Rd increases, a large quantity of thermal energy is released into the system.

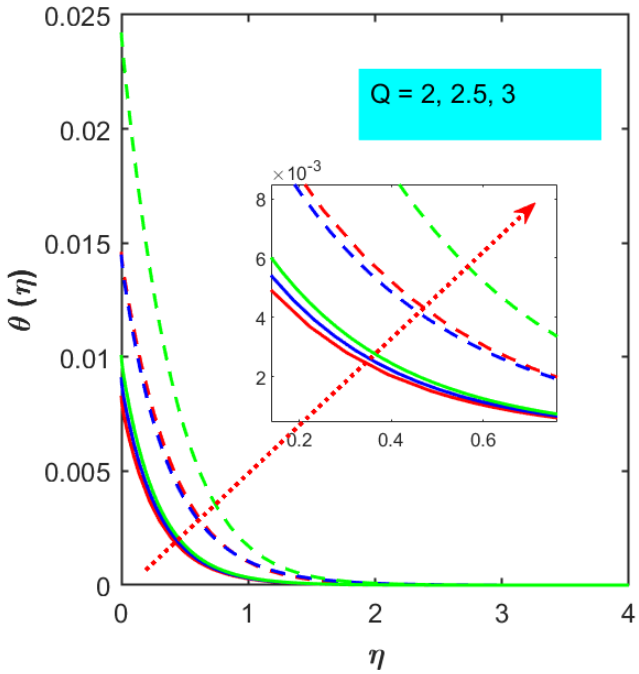


Figure 18. Variation of Q on $\theta(\eta)$.

The impact of the heat source/sink parameter on the temperature plot is seen in Figure 18. Increased radiation absorption causes thermal diffusivity to rise, which reduces the fluid's capacity to transfer heat.

Temperature distribution inside the fluid becomes more noticeable as Q rises, suggesting stronger thermal effects. This trend illustrates how radiative heat transport dominates the modification of the nanofluid's overall thermal profile.

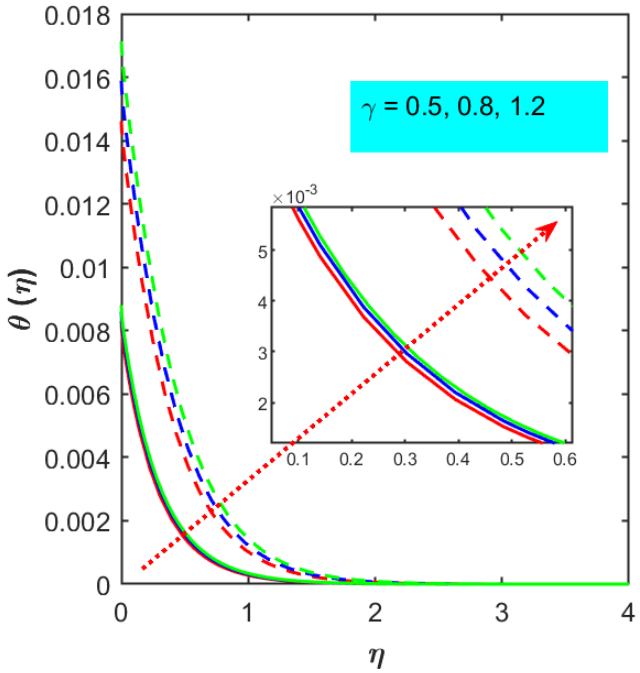


Figure 19. Variation of γ on $\theta(\eta)$.

Figure 19 shows how the temperature profiles are impacted by the γ component in both stretching and shrinking situations. It has been demonstrated that changes in γ significantly affect the fluid's thermal behavior. Heat transmission characteristics are significantly impacted by γ , as seen by the temperature profile rising or falling depending on the flow arrangement.

Figure 20 demonstrates that the ω parameter affects temperature profiles in both stretching and shrinking scenarios. A rise in ω leads to changes in the thermal boundary layer, which affect temperature gradients near the surface. This suggests that the modulation of the heat movement inside the flow field is significantly influenced by ω .

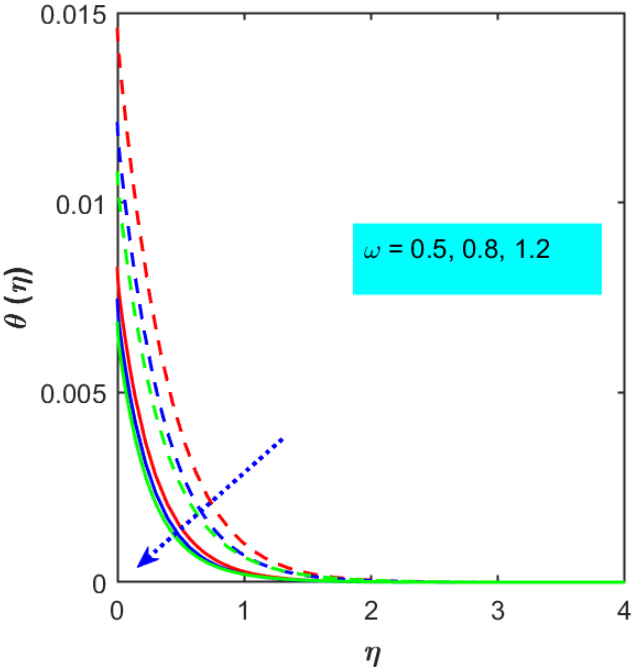


Figure 20. Variation ω of on $\theta(\eta)$.

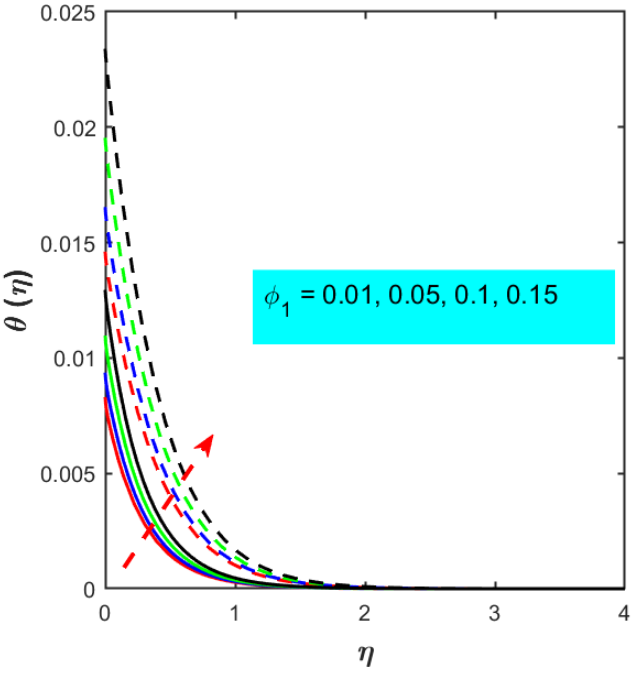


Figure 21. Variation of ϕ_1 on $\theta(\eta)$.

The scientific estimations for base fluid and nanoparticles are displayed in Table 2, whereas Table 1 displays the mathematical computations for the thermophysical characteristics of HNFs. The discussion of non-dimensional variables are addressed in Table 3. The numerical values of $f''(0)$ and $\theta'(0)$ for various values of the volume concentration of nanoparticles are displayed in Tables 4 and 5. In the case of shrinkage, values of $f''(0)$ rise as the concentration of nanoparticles rises, whereas $\theta'(0)$ tends to decrease in the opposite direction. The numerical values of $f''(0)$ and $\theta'(0)$ are displayed for a range of nanoparticle volume concentration values in Tables 6 and 7. In the stretching case, the values of $f''(0)$ drop as the concentration of nanoparticles increases, whereas $\theta'(0)$ exhibits the reverse pattern.

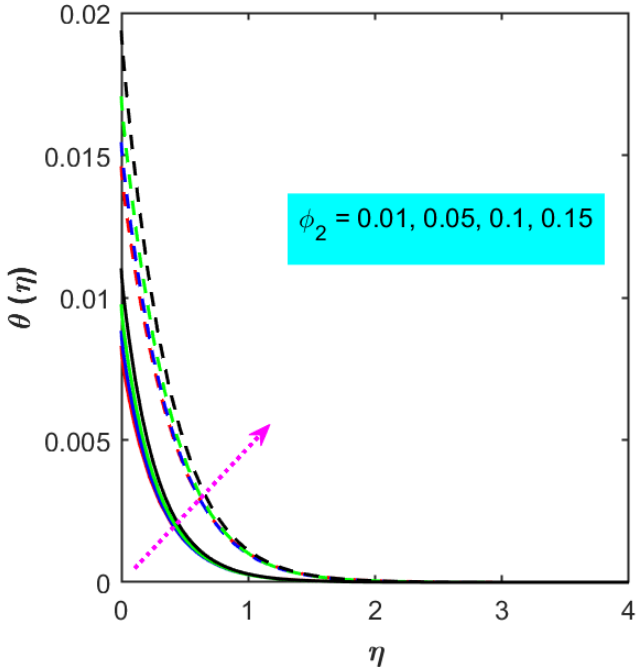


Figure 22. Variation ϕ_2 of on $\theta(\eta)$.

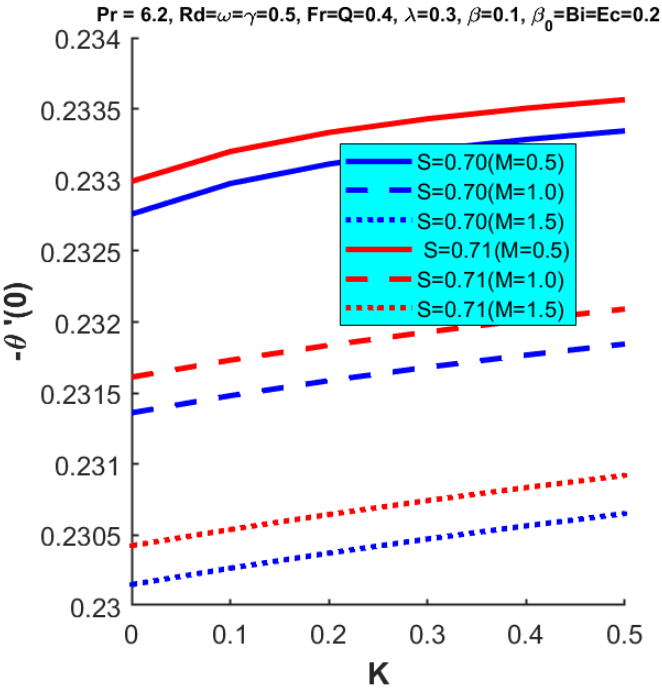


Figure 24. M & S on $-\theta'(0)$.

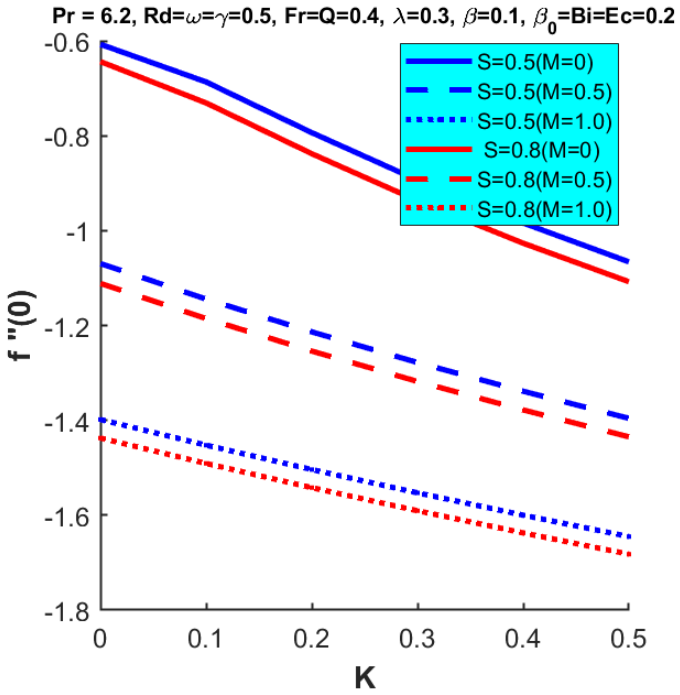


Figure 23. Impact of M & S on $f''(0)$.

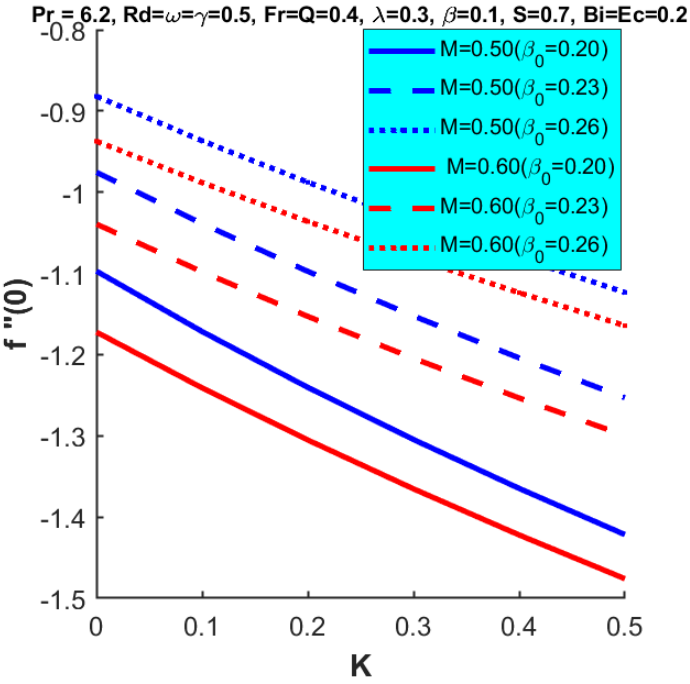


Figure 25. β_0 & M on $f''(0)$.

Table 8 displays the numerical values of $f''(0)$, & $\theta'(0)$ for various λ values. The values of $f''(0)$ fall as λ rises, but $\theta'(0)$ values rise as well. Table 9 shows $f''(0)$, $g''(0)$, & $\theta'(0)$ for different values of Magnetic, Porous, & Suction parameters.

Figures 21 and 22 show that the temperature patterns for stretching situations are affected by the nanoparticle volume concentration component (ϕ_1) . Improved temperature fields result from the nanofluid's improved thermal conductivity as ϕ_1 rises. This suggests that more efficient heat transmission inside the boundary layer is facilitated by greater nanoparticle concentrations.

Figures 23 and 24 plot the skin friction coefficient and russelt number for various M values relative to S. The graphs for a range of M, β_0, Ec , and Fr values are

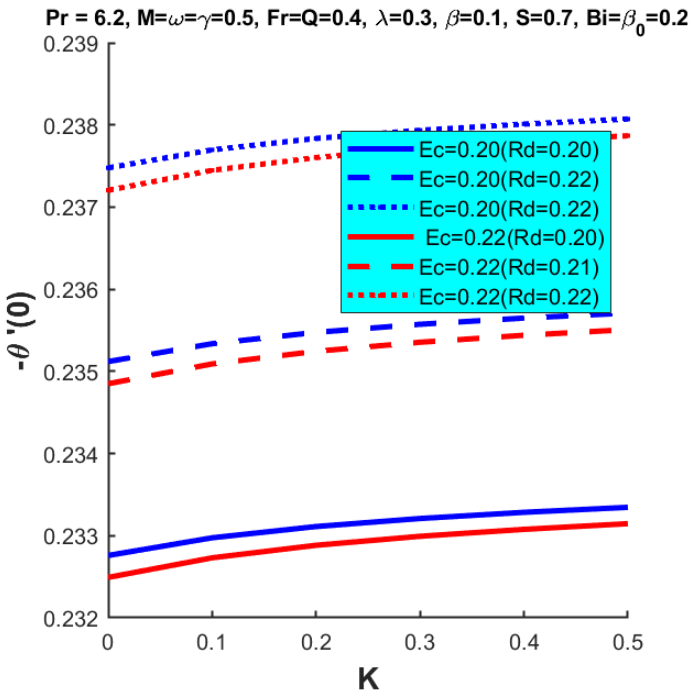


Figure 26. Rd & Ec on $-\theta'(0)$.

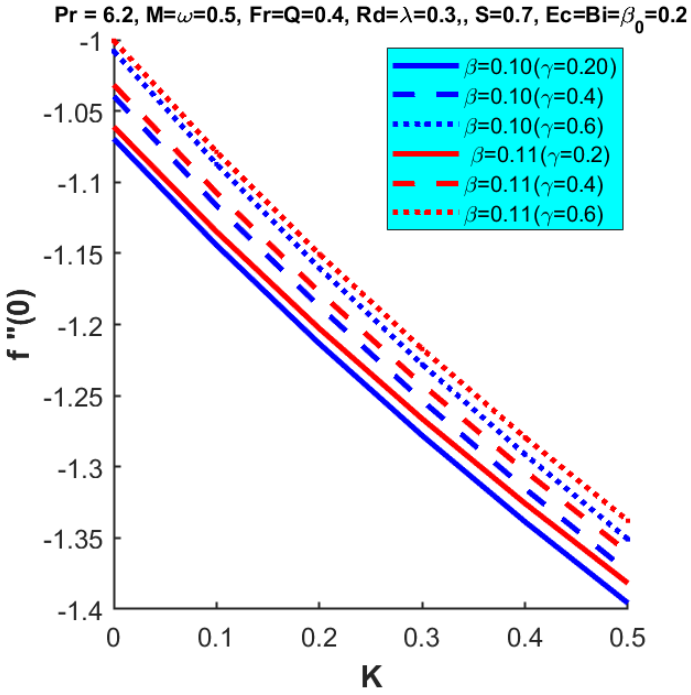


Figure 27. γ & β on $f''(0)$.

displayed in Figures 25, 27, and 29. The graphs for a range of Rd, Ec, Q , and M values are displayed in Figures 26, 28, and 30.

The $f''(0), g''(0), \& \theta'(0)$ numerical findings are displayed in these tables.

Table 4. $f''(0)$ & $\theta'(0)$ for various parameters $\phi_2 = 0, M = 0.1, Fr = 0, \lambda = -1, K = 0, \Pr = 6.2, \beta = 0.1, S = 2, B_0 = 0, Rd = 0, Q = 0, Ec = 0, \Omega = 0.1, \gamma = 0, Bi = 0.1.$

ϕ_1	$f''(0)$	$\theta'(0)$
0.00001	0.370980	-0.991437
0.0001	0.370985	-0.991442
0.001	0.371035	-0.991493
0.01	0.371502	-0.991994
0.1	0.373684	-0.996263

Table 5. $f''(0)$ & $\theta'(0)$ for various parameters $\phi_1 = 0, M = 0.1, Fr = 0, \lambda = -1, K = 0, \Pr = 6.2, \beta = 0.1, S = 2, B_0 = 0, Rd = 0, Q = 0, Ec = 0, \Omega = 0.1, \gamma = 0, Bi = 0.1.$

ϕ_2	$f''(0)$	$\theta'(0)$
0.00001	0.370980	-0.991437
0.0001	0.370985	-0.991441
0.001	0.371035	-0.991486
0.01	0.371502	-0.991927
0.1	0.373684	-0.995894

Table 6. $f''(0)$ & $\theta'(0)$ for various parameters of $\varphi_2 = 0, M = 0.1, Fr = 0, \lambda = 1, K = 0, Pr = 6.2, \beta = 0.1, S = 2, B0 = 0, Rd = 0, Q = 0, Ec = 0, \Omega = 0.1, \gamma = 0, Bi = 0.1.$

ϕ_1	$f''(0)$	$\theta'(0)$
0.001	-0.371035	-0.008404
0.01	-0.371502	-0.008351
0.1	-0.373684	-0.007823

Table 7. $f''(0)$ and $\theta'(0)$ for various parameters of $\phi_1 = 0, M = 0.1, Fr = 0, \lambda = 1, K = 0, Pr = 6.2, \beta = 0.1, S = 2, B0 = 0, Rd = 0, Q = 0, Ec = 0, \Omega = 0.1, \gamma = 0, Bi = 0.1.$

ϕ_2	$f''(0)$	$\theta'(0)$
0.001	-0.371035	-0.008404
0.01	-0.371502	-0.008350
0.1	-0.373684	-0.007815

6 Conclusions

One noteworthy invention is the examined of the behavior of a HNFs on a stretched sheet using a three-dimensional Non-Newtonian model. Fluid flow and heat transport processes can be more accurately and realistically shown by three-dimensional simulations than by conventional 2D systems. The novelty of this study lies in incorporating a non-Newtonian fluid model,

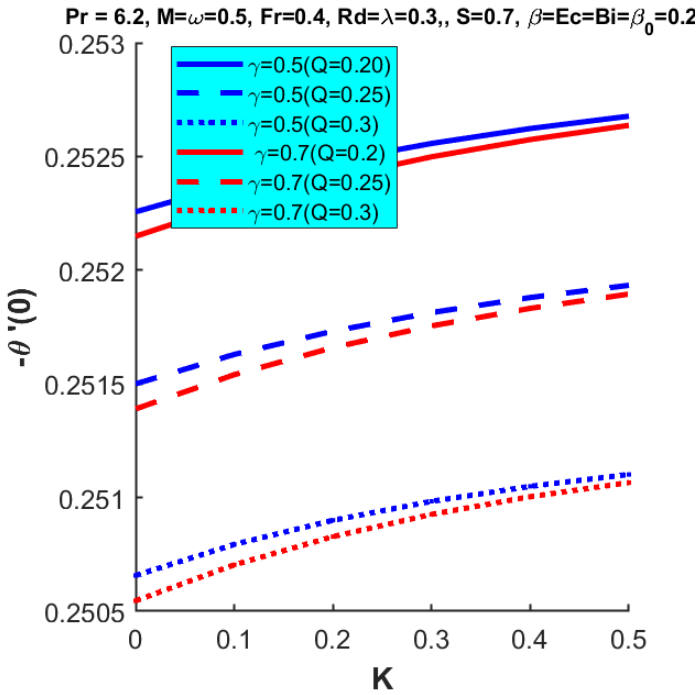


Figure 28. Influence of Q & γ on $-\theta'(0)$.

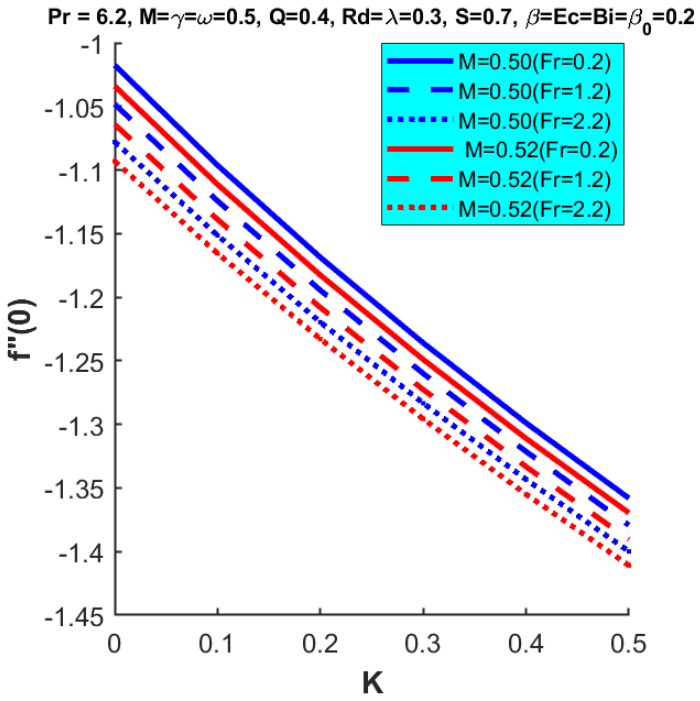


Figure 29. Influence of F_r & M on $f''(0)$.

integrating Darcy-Forchheimer, and Rotating effects in the momentum equations, and including Joule heating and a heat-source parameter in the energy equation.

When the amount proportion of nanoparticles increases, the HNFs viscosity often does as well. When compared to the base fluid alone, nanoparticles

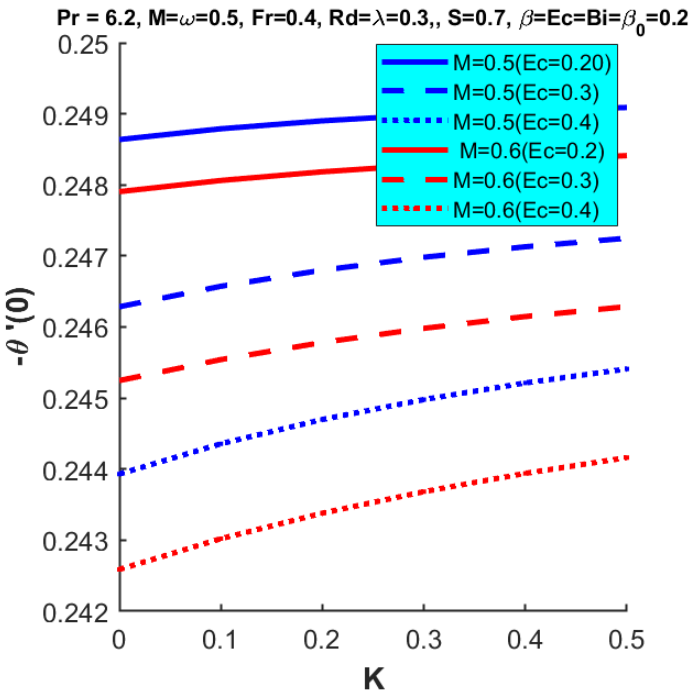


Figure 30. Impact of E_c & M on $-\theta'(0)$.

Table 8. $f''(0)$ and $\theta'(0)$ for various parameters $\phi_1 = \phi_2 = 0.001, M = 0, Fr = 0, K = 0, \Pr = 0, \beta = 0, S = 0, B_0 = 0, Rd = 0, Q = 0, Ec = 0, \Omega = 0.1, \gamma = 0, Bi = 0.$

λ	$f''(0)$	$g''(0)$
0.1	-0.025000	0.100000
0.2	-0.050000	0.200000
0.3	-0.075000	0.300000
0.4	-0.100000	0.400000
0.5	-0.125000	0.500000
0.6	-0.150000	0.600000

Table 9. $f''0)$ & $\theta'(0)$ for various parameters of $\phi_1 = \phi_2 = 0.01, M = 0.1, Fr = 0, \lambda = 0.6, K = 0.1, \Pr = 6.2, \beta = 0.1, S = 0.1, B_0 = 0, Rd = 0, Q = 0, Ec = 0, \Omega = 0.1, \gamma = 0, Bi = 0.1.$

M	K	S	$f''(0)$	$g''(0)$	$\theta'(0)$
0.1	-	-	-0.271403	0.572860	0.038976
0.2	-	-	-0.319841	0.568016	0.039380
0.3	-	-	-0.362252	0.563775	0.039745
-	0.2	-	-0.319440	0.568056	0.039376
-	0.3	-	-0.361542	0.563846	0.039739
-	-	0.2	-0.271403	0.572860	0.033112
-	-	0.3	-0.271403	0.572860	0.028580

increase the flow resistance, which increases viscosity. When a fluid becomes more viscous, its flow rate usually drops. Hybrid nanofluids are formed by dispersing multiple nanoparticles in a base

fluid, which significantly boosts the fluid's thermal conductivity and heat-transfer capability. This enhancement makes them highly useful in cooling, thermal management, and heat-exchange applications.

The following is a summary of the investigation's main conclusions:

- A boundary layer forms near the stretched sheet, and its thickness depends on the fluid velocity. Higher velocity thins the boundary layer, reducing thermal resistance and improving heat transfer between the fluid and the sheet.

- Increasing the volume fraction of hybrid nanofluids in water enlarges the momentum boundary layer while reducing velocity profiles.

- A stronger magnetic parameter further suppresses fluid velocity and enhances the temperature profile.

- When the Casson parameter (β_0) quantities rise, the temperature curve and the velocities under study both fall.

- The velocities and the $\theta(\eta)$ profile under study both drop when the Suction component (S) values rise.

- With increasing levels of the overall amount of nanoparticles component (ϕ_1) , the temperature pattern under studies rises.

- The higher the quantity of the amount of concentration of the nanoparticles parameter (ϕ_2) , the better the temperature pattern under study.

- The investigated temperature pattern and velocities decline as the porous parameter (K) values rise.

- Both the velocities and the temperature profile under investigation decrease when the slip component (β_1) values increase. The velocities and temperature profile under study both rise in tandem with the stretching parameter values.

- When the rotation variable's quantities are enhanced, the velocities and the temperature curve under study both rise.

- The fluids' temperature distribution shows a downward tendency as the Prandtl (Pr) parameter rises, but at a certain point, the behavior shifts.

Data Availability Statement

Data will be made available on request.

Funding

This work was supported without any funding.

Conflicts of Interest

The author declares no conflicts of interest.

AI Use Statement

The author declares that no generative AI was used in the preparation of this manuscript.

Ethical Approval and Consent to Participate

Not applicable.

References

[1] Dey, D., Kumar, P., & Samantaray, S. (2017). A review of nanofluid preparation, stability, and thermo-physical properties. *Heat Transfer—Asian Research, 46*(8), 1413-1442. [Crossref]

[2] Makinde, O. D., & Aziz, A. (2011). Boundary layer flow of a nanofluid past a stretching sheet with a convective boundary condition. *International Journal of Thermal Sciences, 50*(7), 1326-1332. [Crossref]

[3] Malvandi, A., Heysiattalab, S., & Ganji, D. D. (2016). Thermophoresis and Brownian motion effects on heat transfer enhancement at film boiling of nanofluids over a vertical cylinder. *Journal of Molecular Liquids, 216*, 503-509. [Crossref]

[4] Ullah, R., Ali, F., Sheikh, N. A., Alqahtani, S., & Khan, I. (2024). Viscoelastic Dusty Nanofluids containing Nanodiamond in a Rotating Porous Channel. *BioNanoScience, 14*(2), 1456-1472. [Crossref]

[5] Ishak, S. S., Mazlan, N. N., Ilias, M. R., Osman, R., Kasim, A. R. M., & Mohammad, N. F. (2022). Radiation effects on inclined magnetohydrodynamics mixed convection boundary layer flow of hybrid nanofluids over a moving and static wedge. *Journal of Advanced Research in Applied Sciences and Engineering Technology, 28*, 68-84. [Crossref]

[6] Waqas, M., Hayat, T., & Alsaedi, A. (2019). A theoretical analysis of SWCNT–MWCNT and H2O nanofluids considering Darcy–Forchheimer relation. *Applied Nanoscience, 9*(5), 1183-1191. [Crossref]

[7] Mahian, O., Bellos, E., Markides, C. N., Taylor, R. A., Alagumalai, A., Yang, L., ... & Wongwises, S. (2021). Recent advances in using nanofluids in renewable energy systems and the environmental implications of their uptake. *Nano Energy, 86*, 106069. [Crossref]

[8] Daniel, Y. S., Aziz, Z. A., Ismail, Z., & Salah, F. (2018). Effects of slip and convective conditions on MHD flow of nanofluid over a porous nonlinear stretching/shrinking sheet. *Australian Journal of Mechanical Engineering, 16*(3), 213-229. [Crossref]

[9] Nandy, S. K., & Mahapatra, T. R. (2013). Effects of slip and heat generation/absorption on MHD stagnation flow of nanofluid past a stretching/shrinking surface with convective boundary conditions. *International Journal of Heat and Mass Transfer, 64*, 1091-1100. [Crossref]

[10] Sundar, L. S., Sharma, K. V., Singh, M. K., & Sousa, A. C. M. (2017). Hybrid nanofluids preparation, thermal properties, heat transfer and friction factor–a review. *Renewable and Sustainable Energy Reviews, 68*, 185-198. [Crossref]

[11] Aly, E. H., & Pop, I. (2019). MHD flow and heat transfer over a permeable stretching/shrinking sheet in a hybrid nanofluid with a convective boundary condition. *International Journal of Numerical Methods for Heat & Fluid Flow, 29*(9), 3012-3038. [Crossref]

[12] Waini, I., Ishak, A., & Pop, I. (2020). Hybrid nanofluid flow induced by an exponentially shrinking sheet. *Chinese Journal of Physics, 68*, 468-482. [Crossref]

[13] Waini, I., Ishak, A., & Pop, I. (2019). Unsteady flow and heat transfer past a stretching/shrinking sheet in a hybrid nanofluid. *International journal of heat and mass transfer, 136*, 288-297. [Crossref]

[14] Anuar, N. S., Bachok, N., & Pop, I. (2020). Cu-Al2O3/water hybrid nanofluid stagnation point flow past MHD stretching/shrinking sheet in presence of homogeneous-heterogeneous and convective boundary conditions. *Mathematics, 8*(8), 1237. [Crossref]

[15] Ishak, A., Merkin, J. H., Nazar, R., & Pop, I. (2008). Mixed convection boundary layer flow over a permeable vertical surface with prescribed wall heat flux. *Zeitschrift für angewandte Mathematik und Physik, 59*(1), 100-123. [Crossref]

[16] Abdollahi, S. A., Alizadeh, A. A., Zarinfar, M., & Pasha, P. (2023). Investigating heat transfer and fluid flow betwixt parallel surfaces under the influence of hybrid nanofluid suction and injection with numerical analytical technique. *Alexandria Engineering Journal, 70*, 423-439. [Crossref]

[17] Alreshidi, N. A., Shah, Z., Dawar, A., Kumam, P., Shutaywi, M., & Watthayu, W. (2020). Brownian motion and thermophoresis effects on MHD three dimensional nanofluid flow with slip conditions and Joule dissipation due to porous rotating disk. *Molecules, 25*(3), 729. [Crossref]

[18] Kataria, H. R., & Mittal, A. S. (2017). Velocity, mass and temperature analysis of gravity-driven convection nanofluid flow past an oscillating vertical plate in the presence of magnetic field in a porous medium. *Applied Thermal Engineering, 110*, 864-874. [Crossref]

[19] Shah, Z., Sulaiman, M., Dawar, A., Alshehri, M. H., & Vrinceanu, N. (2024). Darcy–Forchheimer MHD rotationally symmetric micropolar hybrid-nanofluid flow with melting heat transfer over a radially stretchable porous rotating disk. *Journal of Thermal Analysis and Calorimetry, 149*(24), 14625-14641. [Crossref]

[20] Waini, I., Ishak, A., & Pop, I. (2020). Flow and heat transfer of a hybrid nanofluid past a permeable moving surface. *Chinese Journal of Physics, 66*, 606-619. [Crossref]

[21] Manjunatha, N., Reddy, M. G., Aloqaily, A., Aljohani, S., Reddy, A. R., Ali, F., & Mlaiki, N. (2025). Radiation effects on rotating system free convective nanofluid unsteady flow with heat source and magnetic field. *Partial Differential Equations in Applied Mathematics, 13*, 101083. [Crossref]

[22] Krishna, M. V., & Reddy, M. G. (2018). MHD free convective boundary layer flow through porous medium past a moving vertical platewith heat source and chemical reaction. *Materials Today: Proceedings, 5*(1), 91-98. [Crossref]

[23] Ali, G., Kumam, P., Sitthithakerngkiet, K., & Jarad, F. (2024). Heat transfer analysis of unsteady MHD slip flow of ternary hybrid Casson fluid through nonlinear stretching disk embedded in a porous medium. *Ain Shams Engineering Journal, 15*(2), 102419. [Crossref]

[24] Hussain, Z., Aljuaydi, F., Ayaz, M., & Islam, S. (2024). Significance of slips and convective conditions towards the non-Newtonian hybrid nanofluid flow over a bi-directional stretching surface. *International Journal of Thermofluids, 21*, 100537. [Crossref]

[25] Ahmad, W., Saqib, M., Khan, I., Oqilat, O., & Khan, M. S. (2025). Significance of Soret Dufour Effects on MHD Mixed Convective Flow of Maxwell Hybrid Nanofluid in Porous Medium with Activation Energy. *International Journal of Thermofluids*, 101278. [Crossref]

[26] Ibrahim, W., & Anbessa, T. (2020). Three-dimensional MHD mixed convection flow of Casson nanofluid with Hall and ion slip effects. *Mathematical Problems in Engineering, 2020*(1), 8656147. [Crossref]

[27] Alnahdi, A. S., & Gul, T. (2023). Hybrid nanofluid flow over a slippery surface for thermal exploration. *Advances in Mechanical Engineering, 15*(8), 16878132231190060. [Crossref]

[28] Zainal, N. A., Nazar, R., Naganthran, K., & Pop, I. (2022). Slip effects on unsteady mixed convection of hybrid nanofluid flow near the stagnation point. *Applied Mathematics and Mechanics, 43*(4), 547-556. [Crossref]

[29] Asghar, A., Chandio, A. F., Shah, Z., Vrinceanu, N., Deebani, W., Shutaywi, M., & Lund, L. A. (2023). Magnetized mixed convection hybrid nanofluid with effect of heat generation/absorption and velocity slip condition. *Heliyon, 9*(2). [Crossref]

[30] Usman, M., Amin, S., & Saeed, A. (2022). Magnetohydrodynamic hybrid nanofluid flow with the effect of Darcy–Forchheimer theory and slip conditions over an exponential stretchable sheet. *Advances in Mechanical Engineering, 14*(8), 16878132221116479. [Crossref]

[31] Haider, F., Hayat, T., & Alsaedi, A. (2021). Flow of hybrid nanofluid through Darcy-Forchheimer porous space with variable characteristics. *Alexandria Engineering Journal, 60*(3), 3047-3056. [Crossref]

[32] Abu Bakar, S., Wahid, N. S., Arifin, N. M., & Khashi'ie, N. S. (2025). The flow of hybrid nanofluid past a permeable shrinking sheet in a Darcy–Forchheimer porous medium with second-order velocity slip. *Waves in random and complex media, 35*(1), 46-63. [Crossref]

[33] Ali, F., Zaib, A., Abbas, M., Anitha, G., Loganathan, K., & Reddy, G. R. (2024). Radiative flow of cross ternary hybrid nanofluid (MoS2, TiO2, Ag/CMC-water) in a Darcy Forchheimer porous medium over a stretching cylinder with entropy minimization. *Heliyon, 10*(14). [Crossref]

[34] Ganesh, N. V., Hakeem, A. A., & Ganga, B. (2018). Darcy–Forchheimer flow of hydromagnetic nanofluid over a stretching/shrinking sheet in a thermally stratified porous medium with second order slip, viscous and Ohmic dissipations effects. *Ain Shams Engineering Journal, 9*(4), 939-951. [Crossref]

[35] Seddeek, M. A. (2006). Influence of viscous dissipation and thermophoresis on Darcy–Forchheimer mixed convection in a fluid saturated porous media. *Journal of Colloid and interface Science, 293*(1), 137-142. [Crossref]

[36] Saeed, A., Tassaddiq, A., Khan, A., Jawad, M., Deebani, W., Shah, Z., & Islam, S. (2020). Darcy-Forchheimer MHD hybrid nanofluid flow and heat transfer analysis over a porous stretching cylinder. *Coatings, 10*(4), 391. [Crossref]

[37] Alzahrani, A. K., Ullah, M. Z., Alshomrani, A. S., & Gul, T. (2021). Hybrid nanofluid flow in a Darcy-Forchheimer permeable medium over a flat plate due to solar radiation. *Case Studies in Thermal Engineering, 26*, 100955. [Crossref]

[38] Alrabaiah, H., Iftikhar, S., Saeed, A., Bilal, M., Eldin, S. M., & Galal, A. M. (2023). Numerical calculation of Darcy Forchheimer radiative hybrid nanofluid flow across a curved slippery surface. *South African Journal of Chemical Engineering, 45*, 172-181. [Crossref]

[39] Devi, S. A., & Devi, S. S. U. (2016). Numerical investigation of hydromagnetic hybrid Cu–Al2O3/water nanofluid flow over a permeable stretching sheet with suction. *International Journal of Nonlinear Sciences and Numerical Simulation, 17*(5), 249-257. [Crossref]

[40] Khashi'ie, N. S., Arifin, N. M., Pop, I., Nazar, R., Hafidzuddin, E. H., & Wahi, N. (2020). Three-dimensional hybrid nanofluid flow and heat transfer past a permeable stretching/shrinking sheet with velocity slip and convective condition. *Chinese Journal of Physics, 66*, 157-171. [Crossref]

[41] Kumar, K. G., Ramesh, G. K., Gireesha, B. J., & Gorla, R. S. R. (2018). Characteristics of Joule heating and viscous dissipation on three-dimensional flow of Oldroyd B nanofluid with thermal radiation. *Alexandria Engineering Journal, 57*(3), 2139-2149. [Crossref]

[42] Ahmed, S., Badak, K., & Sharma, R. P. (2024). Three dimensional hybrid nanofluid along a stretching/shrinking sheet: application of $Al_2O_3 - Cu$. *Latin American Applied Research-An international journal, 54*(2), 277-285. [Crossref]

[43] Iqbal, M. A., Usman, M., Allehiany, F. M., Hussain, M., & Khan, K. A. (2023). Rotating MHD Williamson nanofluid flow in 3D over exponentially stretching sheet with variable thermal conductivity and diffusivity. *Heliyon, 9*(11). [Crossref]

[44] Aldhafeeri, A. A., & Yasmin, H. (2024). A numerical analysis of the rotational flow of a hybrid nanofluid past a unidirectional extending surface with velocity and thermal slip conditions. *Reviews on Advanced Materials Science, 63*(1), 20240052. [Crossref]

[45] Wahid, N. S., Arifin, N. M., Khashi'ie, N. S., Pop, I., Bachok, N., & Hafidzuddin, M. E. H. (2022). Unsteady mixed convective stagnation point flow of hybrid nanofluid in porous medium. *Neural Computing and Applications, 34*(17), 14699-14715. [Crossref]

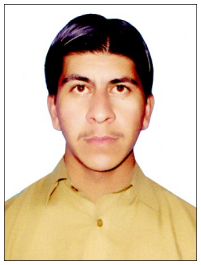
[46] Mahanthesh, B., Gireesha, B. J., & Gorla, R. S. R. (2016). Heat and mass transfer effects on the mixed convective flow of chemically reacting nanofluid past a moving/stationary vertical plate. *Alexandria engineering journal, 55*(1), 569-581. [Crossref]

[47] Shampine, L. F., Kierzenka, J., & Reichelt, M. W. (2000). Solving boundary value problems for ordinary differential equations in MATLAB with bvp4c. *Tutorial notes, 2000*(1-27), 4.

[48] Esfandiari, R. S. (2017). *Numerical methods for engineers and scientists using MATLAB®*. Crc Press. [Crossref]

[49] Hale, N. P. (2006). A sixth-order extension to the matlab bvp4c software of j. kierzenka and l. shampine. *Department of Mathematics, Imperial College London*.

[50] Kierzenka, J., & Shampine, L. F. (2001). A BVP solver based on residual control and the Maltab PSE. *ACM Transactions on Mathematical Software (TOMS), 27*(3), 299-316. [Crossref]



Waqas Ahmad received the M.Phil degree in Applied Mathematics from Qurtuba University of Science & Information Technology Peshawar, Pakistan. (Email: waqas64065@gmail.com)